Non-uniqueness of critical solid fraction considering boundary conditions and strain-rate effects

Investigating the non-uniqueness of critical solid fraction considering boundary conditions and strain rate effects

Mingze Xu[a,b], Zixin Zhang[a,b], Xin Huang[a,b]*, Kevin J. Hanley[c]

[a]Department of Geotechnical Engineering, Tongji University, Shanghai 200092, China

[b]State Key Laboratory of Geotechnical Engineering, Ministry of Education, Tongji University, Shanghai 200092, China

[c]School of Engineering, Institute for Infrastructure and Environment, The University of Edinburgh, Edinburgh EH9 3JL, United Kingdom

*Corresponding author: Tel: +86-021-65982986; Fax: +86-021-65982986; Email: xhuang@tongji.edu.cn

Abstract The critical solid fraction (ϕ_J) which marks the transition between the solid and liquid phases in the jamming diagram is influenced by a number of factors. In this study, the dependency of ϕ_J on strain rate and boundary conditions is examined through Discrete Element Method (DEM) simulations considering a frictionless polydisperse granular system. Different approaches are employed to determine ϕ_J. The observed boundary effect is attributable to the nonuniformity of distribution of solid fraction induced by the clustering tendency of particles close to rigid-wall boundaries at high compression rates. The distribution of solid fraction within the sample in the rigid-wall simulations approaches that in the periodic-boundary simulations as the compression rate decreases. With increasing compression rate, the major force transmission network contains fewer mechanically stable particles and a less stable force transmission network. This causes jamming of the granular assembly at a lower solid fraction. These force transmission networks, however, are fragile and disintegrate quickly upon relaxation.

Keywords: jamming transition; jamming density; strain rate dependency; boundary effects

1 Introduction

Jamming is a broad concept that is related to a variety of phenomena in our daily lives: traffic may become jammed on busy roads; powders may clog when transported through pipes; honey may jam in winter due to a drop of temperature [1]. Jamming is also an important physical concept within granular media that distinguishes the solid phase from the liquid phase: a concept which has been extensively investigated in the past few decades.

A jammed particulate system can sustain external forces without deforming irreversibly. Conversely, an unjammed particulate system may flow if subjected to slight external disturbance [2]. The factors which influence the jamming transition of granular media can be classified into three categories: the structure, dynamical characteristics and thermodynamics [3]. Temperature was thought to be the only factor that influences the transition process until Liu and Nagel [1] pointed out that shear could also lead to a change of packing density, thereby causing a particulate system to jam. Based on this concept, they proposed a jamming diagram which defines jamming and unjamming zones in the temperature-shear stress-solid fraction space. Various extensions of the Liu-Nagel diagram have been proposed. For example, Ciamarra et al. [4] introduced friction as the third coordinate axis in the jamming diagram with zero temperature to incorporate the dependency of jamming transition on friction. Bi et al. [2] found a richer set of behaviors of granular media at zero temperature, based on which they further divided the Liu-Nagel diagram into an unjamming zone, a shear jamming zone, a fragile zone and a jammed zone.

These interpretations share a common key concept: the critical solid fraction, or jamming density, ϕ_J. A

granular system can jam without external disturbance when its solid fraction is above ϕ_J. In contrast, a granular system may unjam and flow when its solid fraction is below ϕ_J. Factors that may influence ϕ_J including loading rate, particle size distribution, particle shape, particle compressibility, friction and the stress path [4-9]. Controversial observations have been reported regarding the dependency of ϕ_J on loading rate. Hartley and Behringer [10] carried out a Couette shear experiment on assemblies of photoelastic disks and found a logarithmic correlation between the internal stresses and shearing rate. However, when they changed the loading mode from shearing to isotropic compression, they found no dependency of the internal stresses on loading rate. Zhang and Makse [11] used molecular dynamics simulations to show that different compression rates resulted in different values of ϕ_J. Mari et al. [12] compared jamming transition with glass transition and found that both showed a clear compression rate dependency, i.e., ϕ_J increases with decreasing compression rate. Similar observations were made by Donev et al. [13], Speedy [14] and Ogarko & Luding [15]. Vågberg et al. [16] found that isotropic compression can result in a large range of ϕ_J related to the compression rate and initial configuration. They showed that the influence of initial state persists even at an extremely slow compression rate. They also found that shearing can only yield a small range of ϕ_J compared with isotropic compression, and at infinitesimally slow shearing rates there exists a well-defined value of critical solid fraction ϕ_J^{QS} that is independent of initial configuration. Otsuki and Hayakawa [17] repeated the shearing and relaxation process in their numerical simulations and found that the hysteresis loops formed are independent of the shearing rate. However, to the best of our knowledge, no prior study has satisfactorily explained the fundamental mechanisms underlying the strain-rate dependency of ϕ_J. In addition, the simulations mentioned above were all performed under periodic boundary conditions; however, in many physical experiments, the sample is bounded by walls that are much stiffer than particles. According to Marketos & Bolton [18] amongst others, rigid-wall boundaries can cause the inhomogeneity of both packing density and strain field. Therefore, it is also important to investigate how the boundary can influence the jamming transition.

In this study, a series of DEM simulations are conducted under both periodic and rigid-wall boundary conditions at a variety of compression rates. Microscopic analyses enable investigation of the particle-scale mechanism underlying the influence of boundary conditions and strain rate on the critical solid fraction.

2 Numerical model

The rigid-wall simulations were run using the well-known commercial software PFC 3D [19]. The periodic-boundary simulations were conducted using the open-source LAMMPS code [20]. A uniform strain rate field (affine transformation) is imposed on the particles in a periodic cell, whereas the displacement of rigid walls only directly affects particles in contact with the walls. 20000 non-contacting frictionless spherical particles were generated within a cubic box bounded by rigid walls at an initial solid fraction (ϕ_0) of 0.05, while 20186 non-contacting particles were placed within a cubic periodic cell with ϕ_0=0.5. We verified that the simulation results using periodic boundaries are insensitive to ϕ_0. Therefore, a higher ϕ_0 was adopted for PB simulations than for RW simulations in order to reduce the simulation time. The polydisperse particle size distribution follows that of Toyoura sand (Figure 1) which has a size ratio between the largest and the smallest particles of 3.55. The particle density was 2650 kg/m^3 without consideration of gravity. A linear elastic model was adopted with a normal contact stiffness (k_n) of 1×10^8 N/m and a tangential contact stiffness (k_s) of 6.67×10^7 N/m. A global (background) damping ratio of 0.1 was adopted in order to reduce the kinetic energy. For both boundary conditions, the sample was isotropically compressed at eight different compression rates (v), i.e., 0.025, 0.25, 2.5, 5, 10, 15, 20 or 25 m/s, until a jammed state was reached. Simulations with periodic boundaries were labelled with initials of PB, while rigid-wall boundaries were labelled with initials of RW. Following [8,9], a

dimensionless compression rate $v_r = v/v_{ref}$ is defined to describe the relative loading rate between different simulations, where v_{ref} is the slowest compression rate 0.025 m/s. Hence v_r ranges from 1-1000. In the PB simulations, the sample was firstly compressed until the solid fraction ϕ=0.63; in the RW simulations, the sample was compressed until ϕ=0.6. These pre-relaxation solid fractions differed because the critical range following this protocol was 0.6-0.62 in the RW simulations but was larger than 0.63 in the PB simulations. Although the ϕ_J value can be influenced by the initial state of the sample [13], the major concern of the current study is the variation of ϕ_J with compression rate which will not be influenced by initial ϕ values for different boundary conditions. The samples were then relaxed until a nearly non-contacting condition was reached, after which the samples were compressed again at the selected compression rates until the jamming state was reached. Finally, in order to remove the dynamic influence, the jammed samples were then decompressed to the unjammed state.

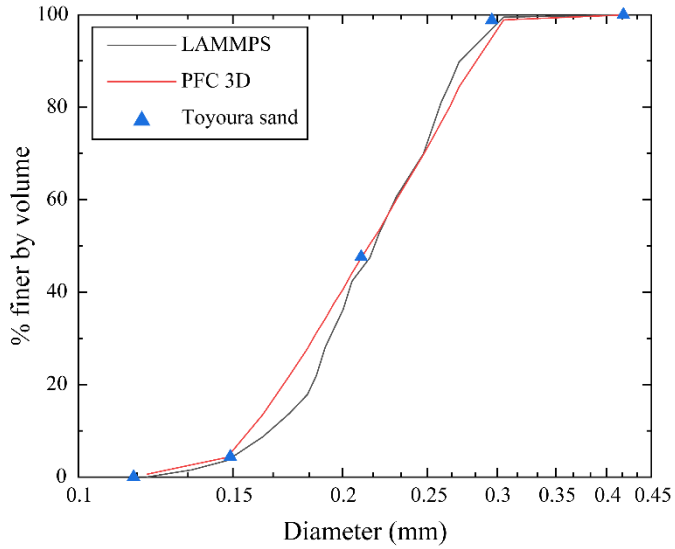

Figure 1 Comparing the particle size distributions of DEM samples and real Toyoura sand

3 Results

3.1 Determination of critical solid fraction

3.1.1 Energy-based criterion

Following Göncü et al. [8], we calculated the energy ratio, $e = E_k/E_p$, to quantify the dynamic effect during both compression and decompression, in which E_k is the kinetic energy and E_p is the potential energy. The evolution of e for two representative simulations is given in Figure 2 for the PB and RW samples, respectively. We also used the energy-based approach proposed by Göncü et al. [8] to determine the critical solid fraction, i.e., jamming transition occurs when the compression e-ϕ curve crosses the decompression e-ϕ curve. It can be seen from Table 1 that for PB simulations, the kinetic energy is small in comparison to the potential energy for all loading rates, which indicates that the dynamic effect is insignificant. The identified ϕ_J decreases consistently with increasing loading rate, which is in accordance with Ogarko and Luding [15] amongst others. However, for RW simulations, e could only remain at a small level when v_r is below 10. In particular, the kinetic energy exceeds the potential energy when v_r is higher than 400, after which the dynamic influence plays a significant role. Therefore, ϕ_J oscillates with v_r without showing a consistent variation trend.

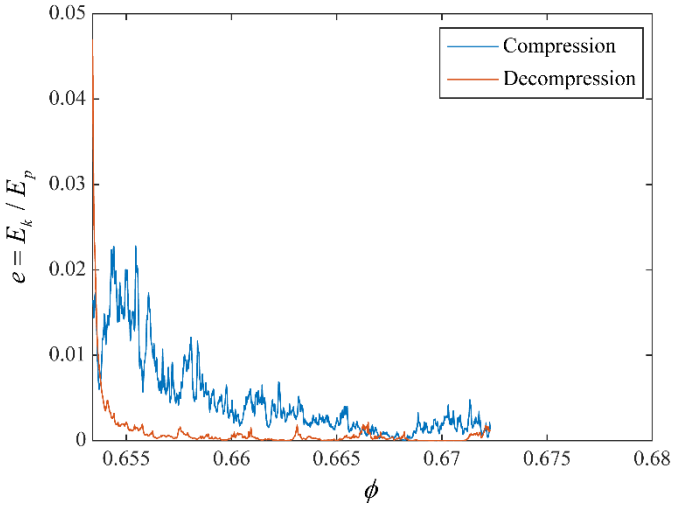

(a) PB (v_r =10)

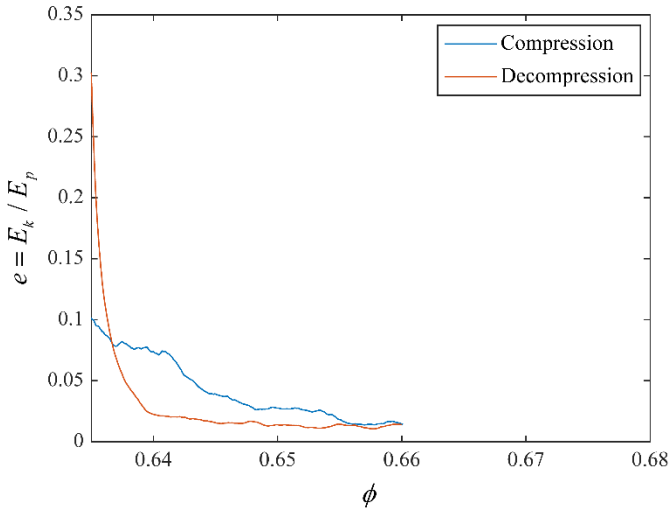

(b) RW (v_r =10)

Figure 2 Ratio of kinetic to potential energy as a function of solid fraction

Table 1 Critical solid fraction determined using the energy-based criterion

Boundary condition	v_r	e	ϕ_J
PB	1	0.0001186	0.6548
	10	0.007462	0.6538
	100	0.0798	0.6519
	200	0.1483	0.6522
	400	0.2316	0.6514
	600	0.3209	0.6506
	800	0.3744	0.6505
	1000	0.3367	0.6506
RW	1	0.02793	0.6359
	10	0.08074	0.6367
	100	0.6848	0.6371
	200	0.7296	0.647
	400	1.165	0.6468
	600	3.369	0.6085
	800	2.699	0.6149
	1000	3.219	0.6151

3.1.2 Pressure-based criterion

For a DEM simulation, the global average stress tensor $\bar{\sigma}$ can be calculated as:

$$\bar{\sigma} = \frac{1}{V}\sum_{p \in V} V^p * \sigma_{ij}^p + \frac{1}{2V}\sum_{p \in V} m^p v_i^p v_j^p \qquad (1)$$

in which V and V^p are the sample volume and particle volume, respectively, σ_{ij}^p is the stress component of an individual particle, m^p is the mass of a particle with velocity v^p. The two terms on the right of Eq. 1 are the

Cauchy and Reynolds stress tensors, respectively. Although the compression rate is relatively large in some simulations, the contribution of Reynolds stress to the overall mean stress is small (for RW samples, the largest contribution is 1.5% for RW-8 while for PB samples, the largest contribution is 0.65% for PB-8). The isotropic mean stress P is:

$$P = tr(\bar{\boldsymbol{\sigma}}) / 3 \tag{2}$$

Following [7], P is normalized by $2\langle r\rangle/k_n$ to get a dimensionless pressure p. $\langle r\rangle$ is the mean particle radius of 0.125 *mm*.

The development of p during isotropic compression and decompression is shown in Figure 3. For the compression process, as v_r increases from 1 to 1000, p becomes larger at the same solid fraction. However, the curves of RW samples begin at a smaller solid fraction and increase more slowly than those of PB samples. Here, the solid fraction corresponding to the first observation of non-zero p cannot be treated as a jamming transition point, as it has been noted both experimentally [21] and numerically [7] that this point does not exactly match the one determined from coordination number. Furthermore, for the RW samples, when v_r exceeds 10, the ϕ-p relationship no longer follows a power-law trend after jamming transition (closer to a straight line), whereas a power-law correlation holds consistently for the PB simulations. The former is probably due to the increasing dynamic effect. For the decompression process, for both boundary conditions a slower v_r leads to a larger ϕ at which p firstly reaches 0. Furthermore, for RW samples, the stress in the samples with $v_r \geq 400$ cannot be fully relaxed even after it has been decompressed to its original state with ϕ=0.6.

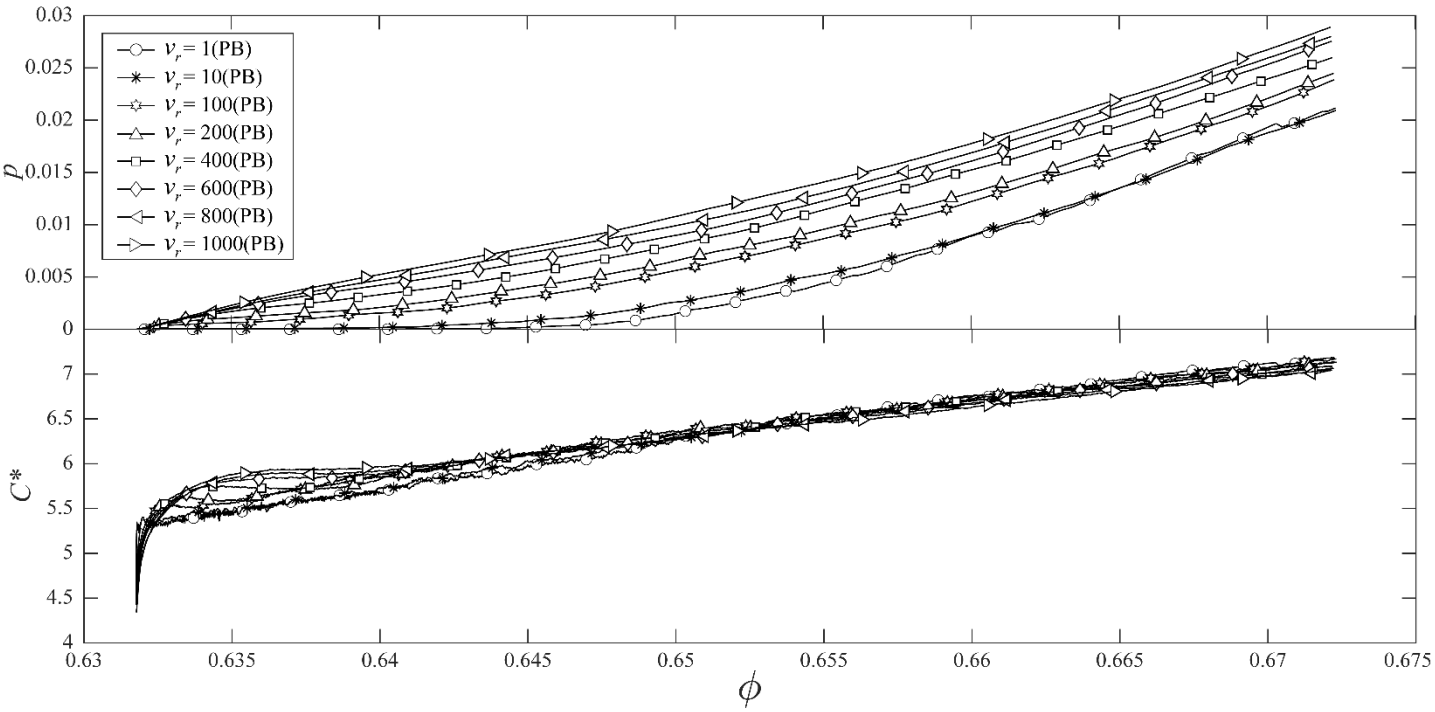

(a) Compression under PB conditions

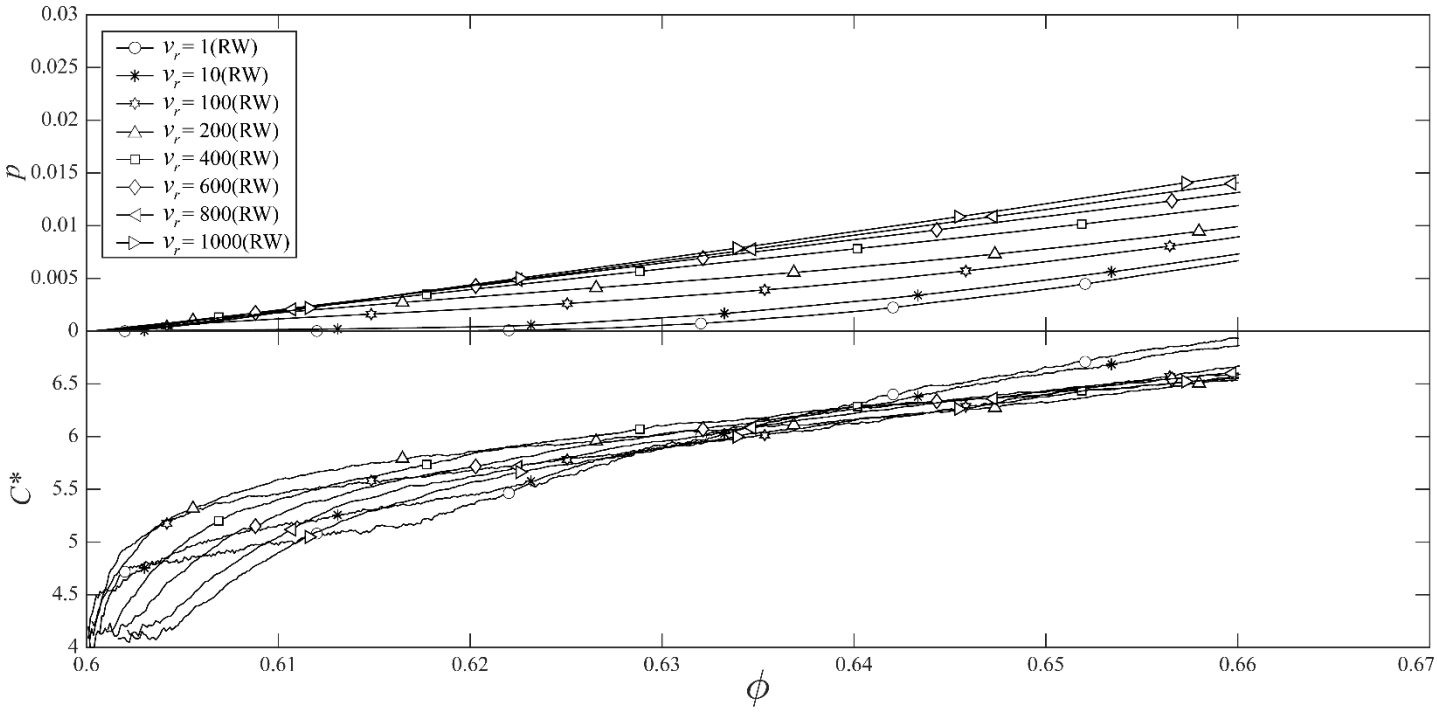

(b) Compression under RW conditions

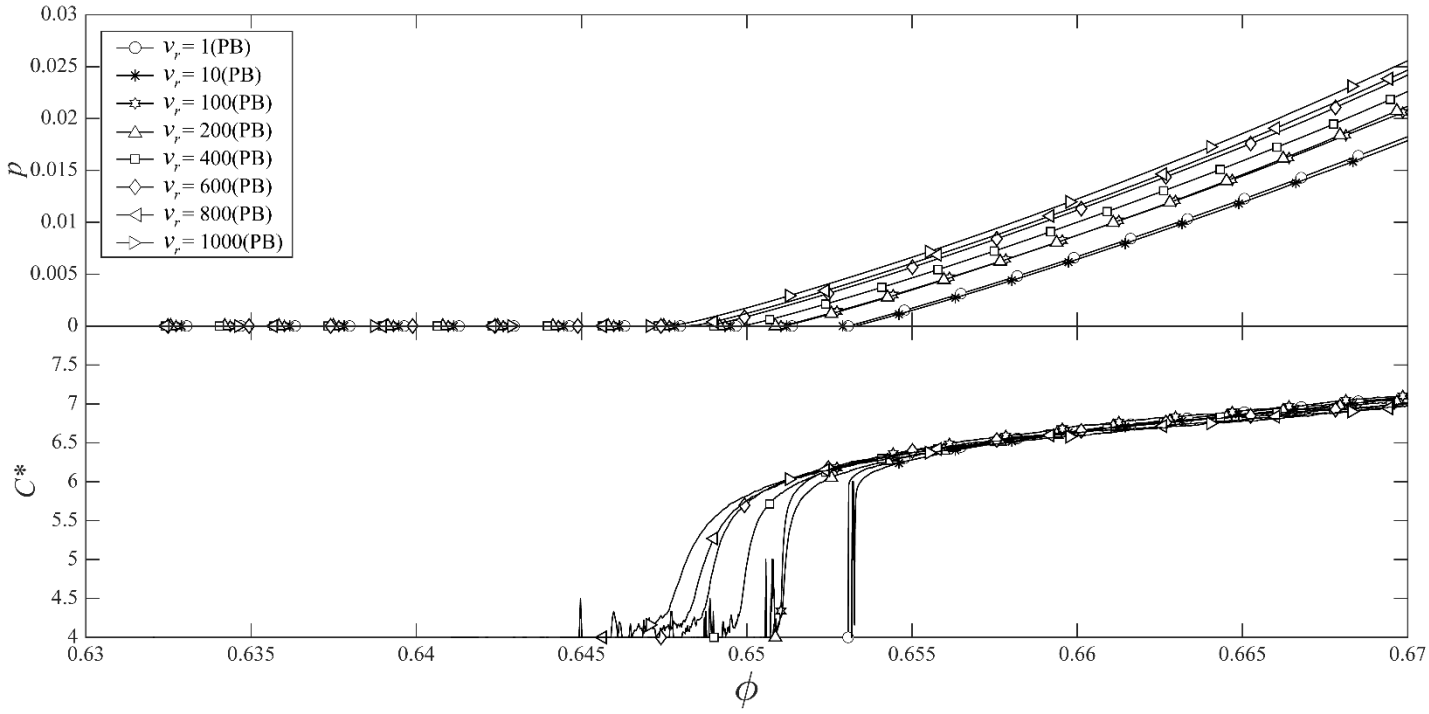

(c) Decompression under PB conditions

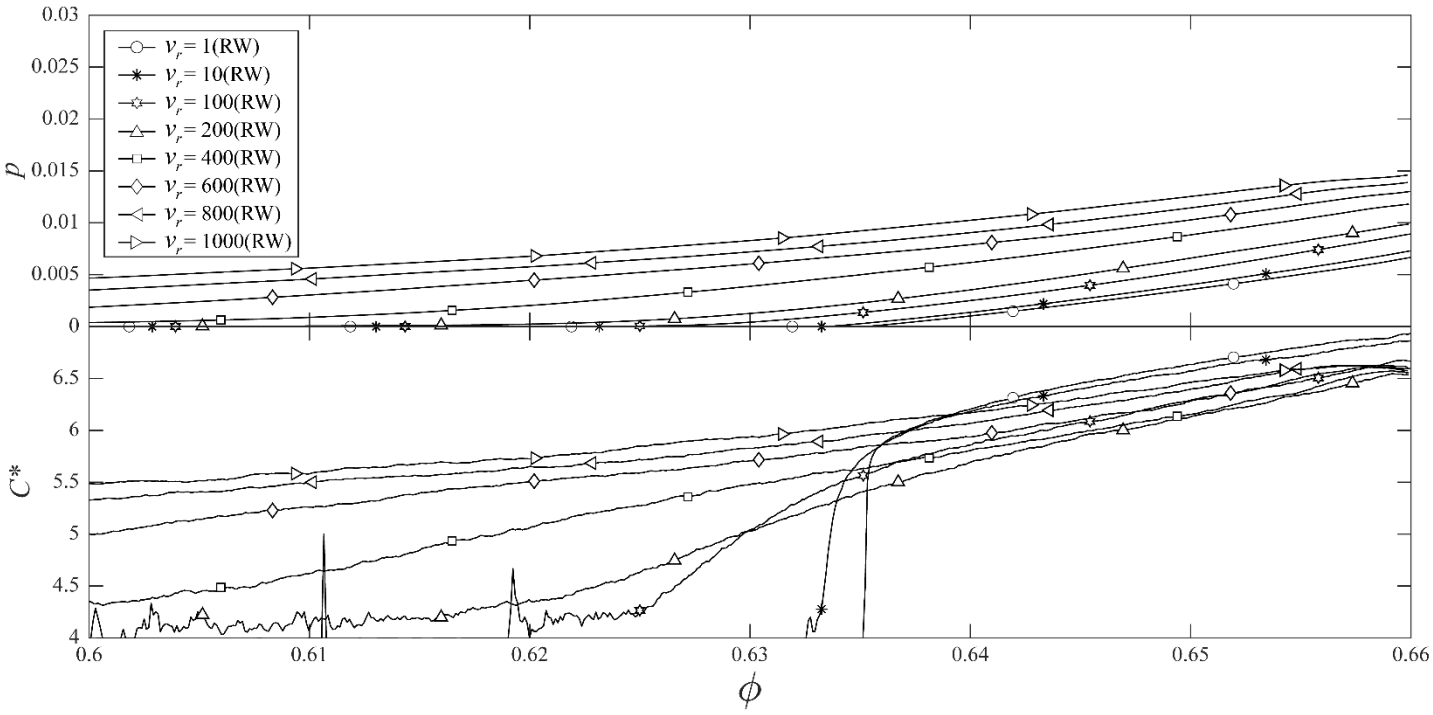

(d) Decompression under RW conditions

Figure 3 Variation of dimensionless p and C^* against ϕ for different boundary conditions

3.1.3 Coordination number-based criterion

The coordination number C^r (Eq. 3) is commonly used to quantitatively describe the contact condition between particles.

$$C^r = \frac{M}{N} \tag{3}$$

in which M is twice the total number of contacts, N is the total number of particles. However, C^r includes the rattlers that make no contribution to major force transmission. The corrected coordination number C^* was proposed by Imole [22] to quantify the mechanically stable contacts.

$$C^* = \frac{M_4}{N_4} \tag{4}$$

M_4 is the total number of contacts owned by the N_4 mechanically stable particles which have at least 4 contacts. Note that the contacts between rigid walls and particles are eliminated when calculating (3) and (4). Following Kumar & Luding [7], we use C^* herein to neglect the influence of rattlers (particles with fewer than 4 contacts). The bottom subfigure of Figure 3 shows C^* against ϕ at different v_r during both compression and decompression processes. In the compression process, C^* is initially smallest for simulations with high v_r (close to the minimum theoretical value of 4 for 3D problems). However, these simulations have the fastest rate of increase of C^* with increasing solid fraction. Nonetheless, in the decompression process, the faster the v_r is, the earlier C^* drops to 4. Theoretically, the isostatic threshold of C^* is 6 for frictionless particles. We adopt this as one criterion to analyze whether or not the sample reaches the isostatic (jamming) state. As pointed out by [8], the pressure-based criterion is more appropriate for the analysis of strain rate dependency, while the coordination number-based method is suitable for a decompression process under PB conditions in which pressure drops to zero when the particle system changes from the jammed state to the unjamming state. The relationship between p, C^* and ϕ can be fitted using

$$\frac{p}{C^*\phi} = p_{ref}\log\left(\frac{\phi}{\phi_J}\right) \quad (5)$$

where ϕ_J and p_{ref} are fitting parameters.

The value of ϕ_J is extracted from Figure 3, which corresponds to the jamming state (C^*=6) at different compression rates. During the decompression process, ϕ_J can be also calculated using Eq. 5 for PB conditions. Although Eq. 5 is originally derived for PB simulations, the RW data also follow Eq. 5. ϕ_J values for RW simulations are also given in Figure 4(b) for comparison. However, it should be noted that some of these ϕ_J values are smaller than ϕ_0=0.6 when v_r exceeds 600. As is shown in Figure 4(a), for the RW samples, there is no consistent trend in the evolution of ϕ_J with v_r. For the PB condition, a clear strain rate dependency can be observed, i.e., ϕ_J decreases with the increasing v_r. Figure 4(b) shows that under decompression conditions, ϕ_J still increases with decreasing v_r for PB simulations. The ϕ_J values identified using different criteria are approximately the same, especially under low loading rates. However, for the RW samples, the ϕ_J values identified from the coordination number-based approach are obviously larger than those determined from the pressure-based criterion. These differences reduce as v_r decreases. Figure 4 indicates that for RW conditions, Eq. 5 can be used only when the compression rate is slow enough, which is associated with a more homogeneous structure and deformation field.

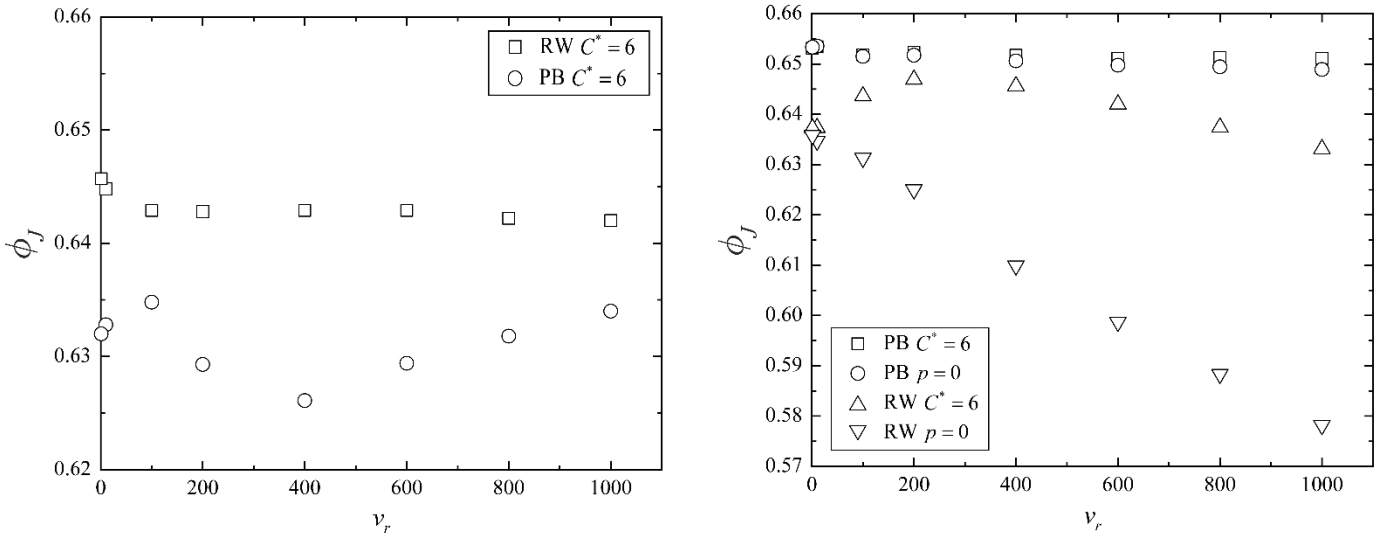

(a) Compression (b) Decompression

Figure 4 Variation of critical solid fraction with compression rate

After the jamming transition point, C^* follows a power-law distribution, i.e., $\left(C^* - C_J^*\right) \propto \left(\phi - \phi_J\right)^\beta$ with C_J^*=6 (Figure 5). Under the decompression condition (Figure 5(a)), $0.5443 \leq \beta \leq 0.6611$ for the PB samples, which is similar to literature results [8,9,21], while for the RW samples β has a larger range with $0.6985 \leq \beta \leq 1.12$. The smallest β value corresponds to the slowest compression rate and is close to the β values obtained in PB simulations, which indicates that the boundary effect is reduced as the compression rate decreases (Figure 5(b)). The compression data also follow power-law correlations but with comparatively larger β values, e.g., for the PB simulations $0.8185 \leq \beta \leq 0.9947$, while for the RW simulations $0.8067 \leq \beta \leq 1.154$. The larger β values correspond to higher dynamic effects under compression than under decompression.

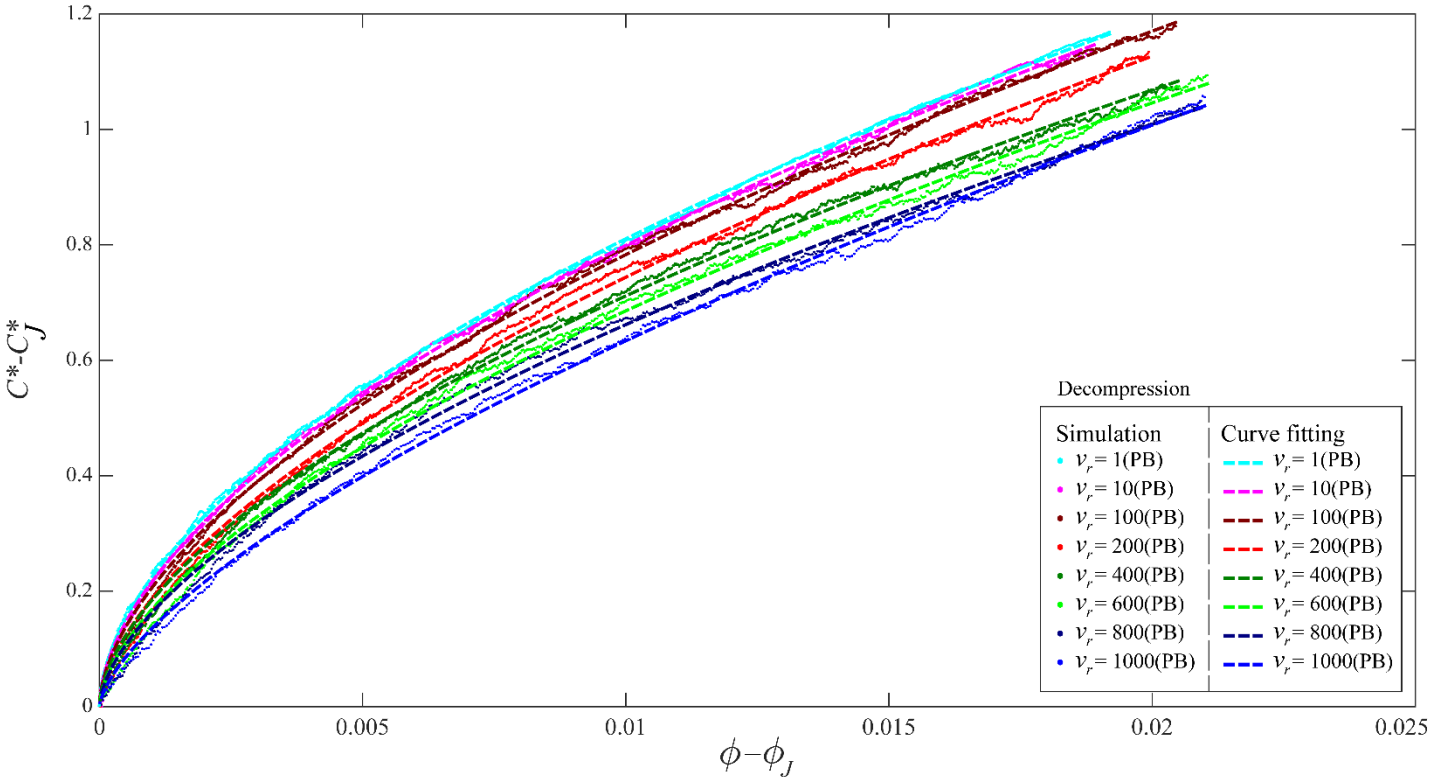

(a) PB decompression

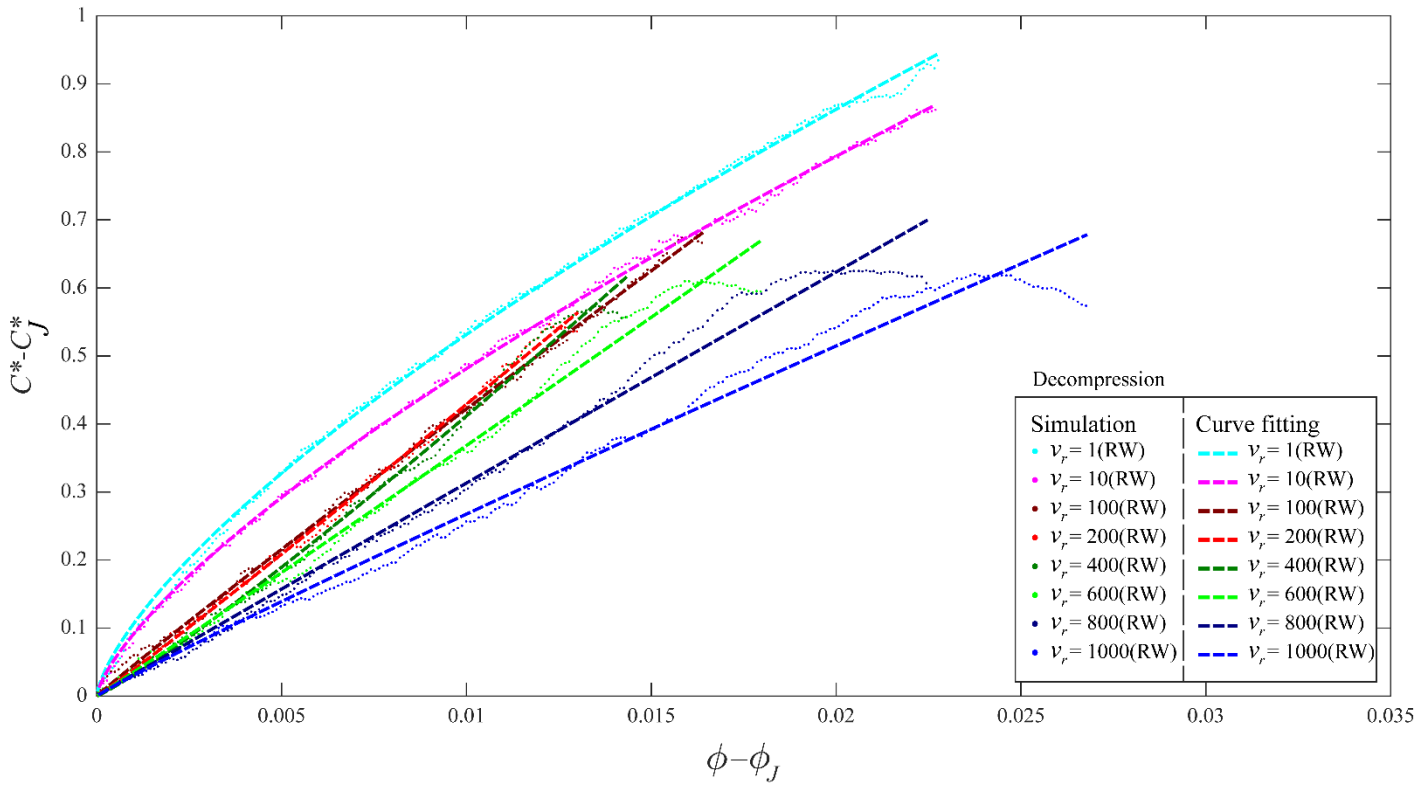

(b) RW decompression

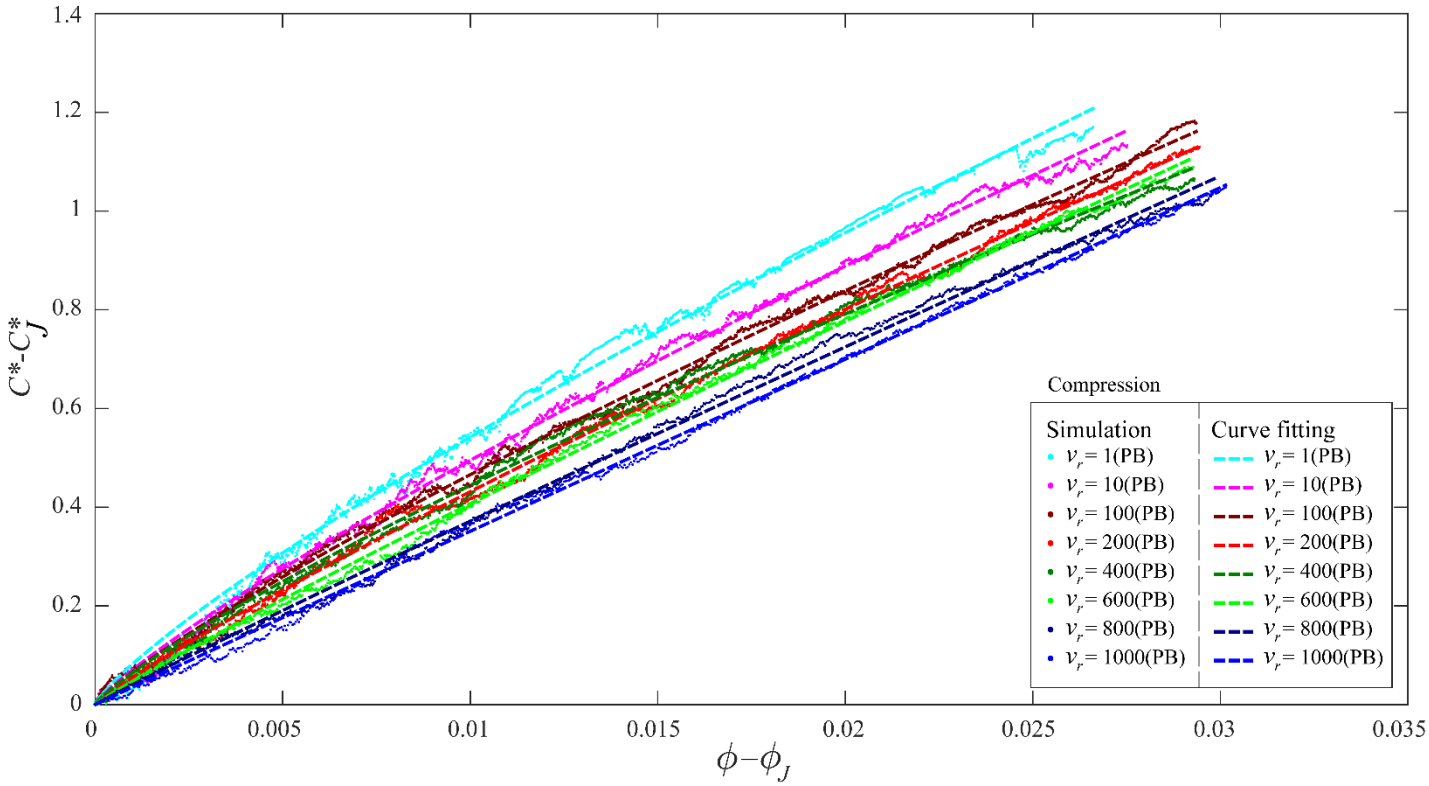

(c) PB compression

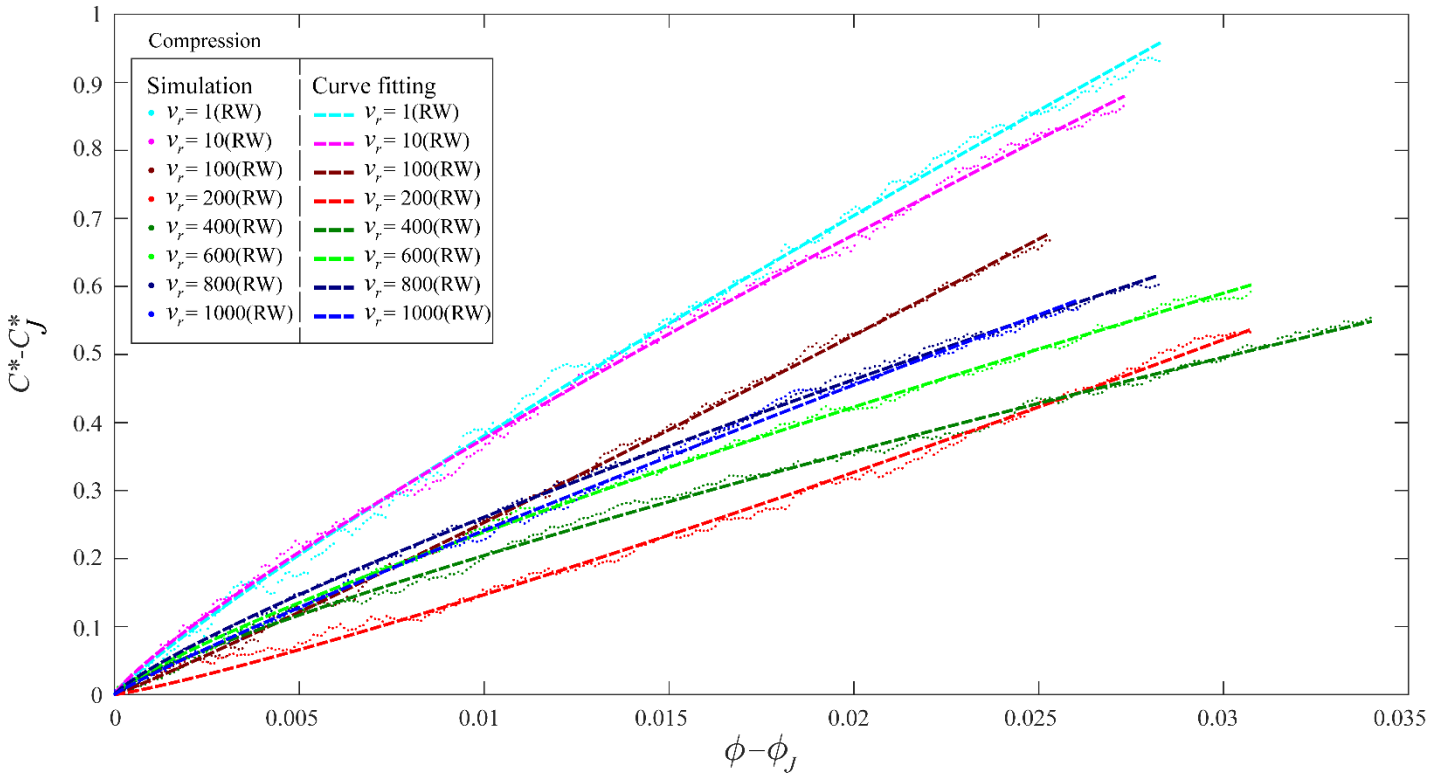

(d) RW compression

Figure 5 Correlations between $C^* - C_J^*$ and $\phi - \phi_J$

To eliminate the influence of different starting points of solid fraction, p is plotted against C^* (Figure 6). As the compression rate decreases, the RW curves approach the PB curves, indicating that the boundary condition has a smaller influence at slower compression rates.

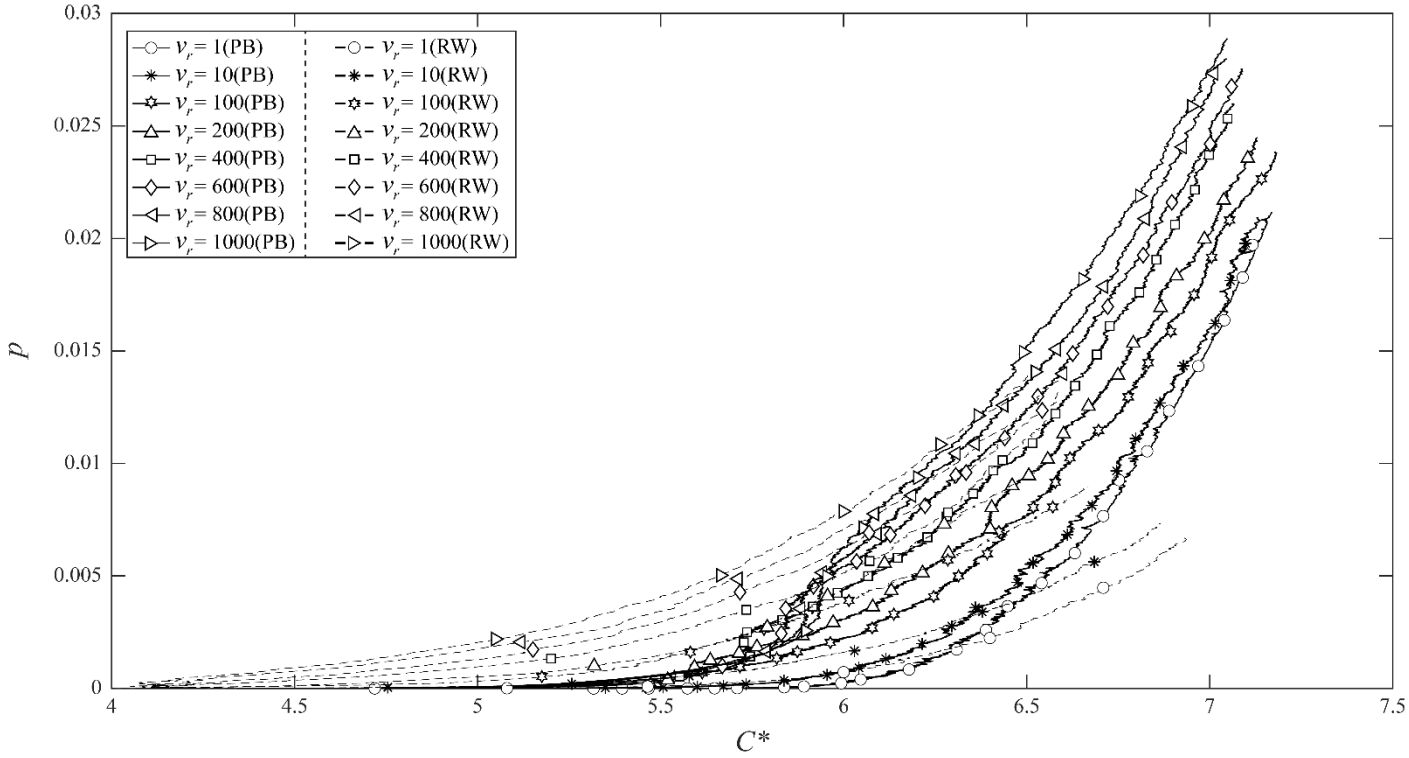

(a) Compression

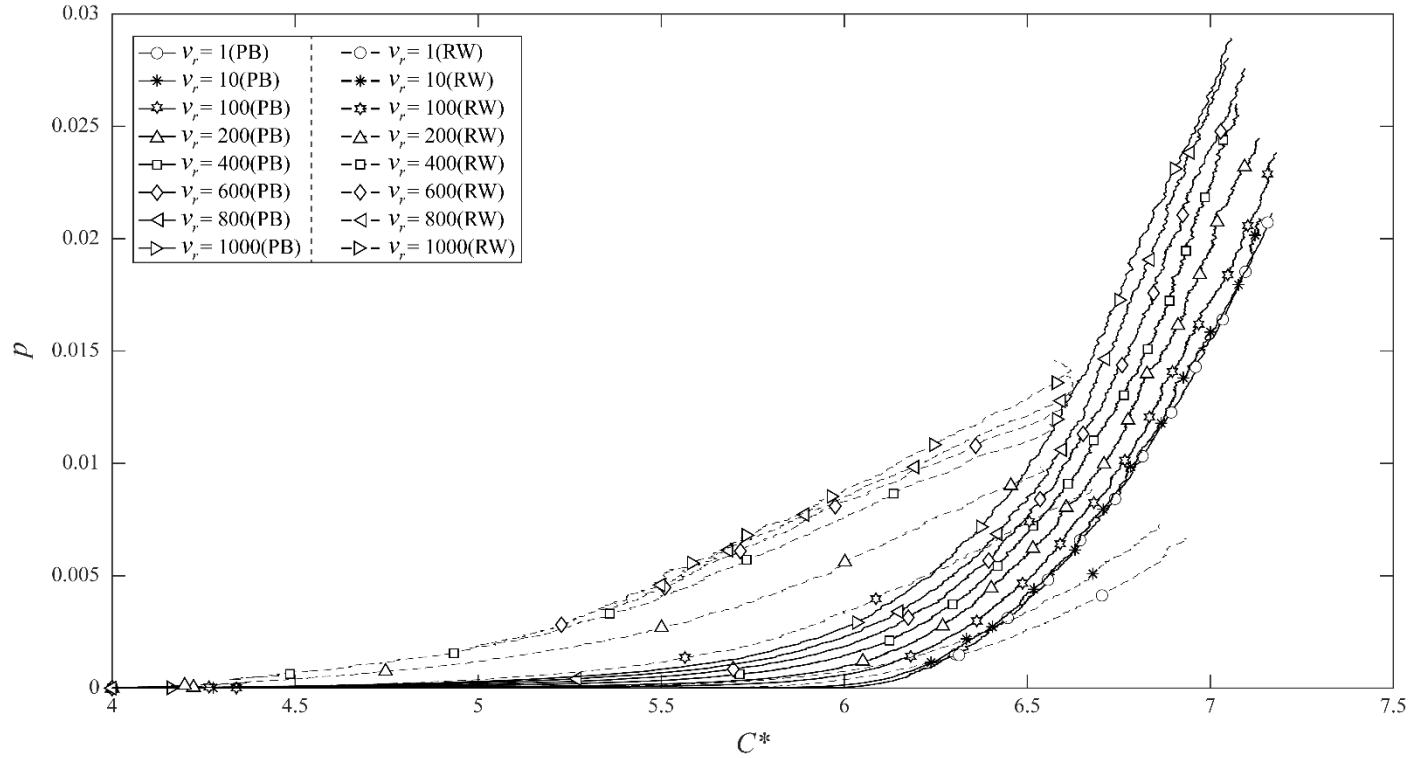

(b) Decompression

Figure 6 Dimensionless p vs C^* for different boundary conditions

3.2 Percolation analysis

Apart from the aforementioned three criteria, Bi et al. [2] also proposed using percolation analysis as a more practical approach. The jammed state is reached when x, y, z directions all come to a percolated state, i.e., $\frac{\xi_x}{L_x} = 1$, $\frac{\xi_y}{L_y} = 1$, $\frac{\xi_z}{L_z} = 1$, where ξ_i is the length of the largest force transmission network and L_i is the sample dimension in the i direction. Following [2], only clusters comprised of strong contacts, i.e., those contacts bearing contact forces $f \geq kf_{avg}$, are considered in percolation analysis as the contribution of the weak force transmission network with $f < kf_{avg}$ to the overall force transmission is negligible [17]. It was shown that, different from k = 1 for 2D frictionless disks [2], k equals 2.2 for 3D frictionless spheres [24-25].

Figure 7 gives an example of percolation analysis with k = 2.0, 2.1 or 2.2 for the PB simulation with v_r=1 during compression. Percolation analyses on other samples under the PB condition during compression are similar and are not given for conciseness. When k=2.0, ξ_i/L_i fluctuates when ϕ is smaller than 0.64, after which $\frac{\xi_i}{L_i} = 1$ in all three directions. The major difference between the current study without shearing and Bi et al. [2] is that during shearing, the force transmission network tends to fully percolate firstly along the deviatoric loading direction and then propagates to the lateral boundaries, while theoretically in isotropic compression $\frac{\xi_i}{L_i} = 1$ should be reached simultaneously in all three directions. The threshold value for the $\frac{\xi_i}{L_i} = 1$ state with k=2.1 is slightly larger than that with k=2.0. However, when k=2.2 there is no stable state of percolation and the ξ_i/L_i values continue to fluctuate. Percolation analysis on the same sample during decompression is shown in Figure 8. In contrast to that during compression, during decompression ϕ at the transition point is nearly the same for k=1.0 and k=2.2 with little fluctuation.

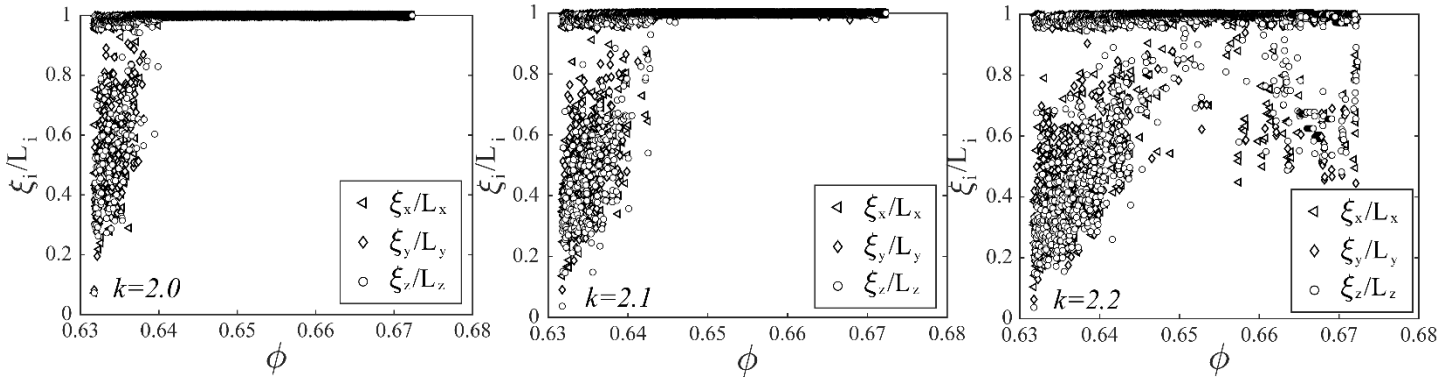

Figure 7 Percolation analysis with different k at v_r=1 during compression for PB conditions

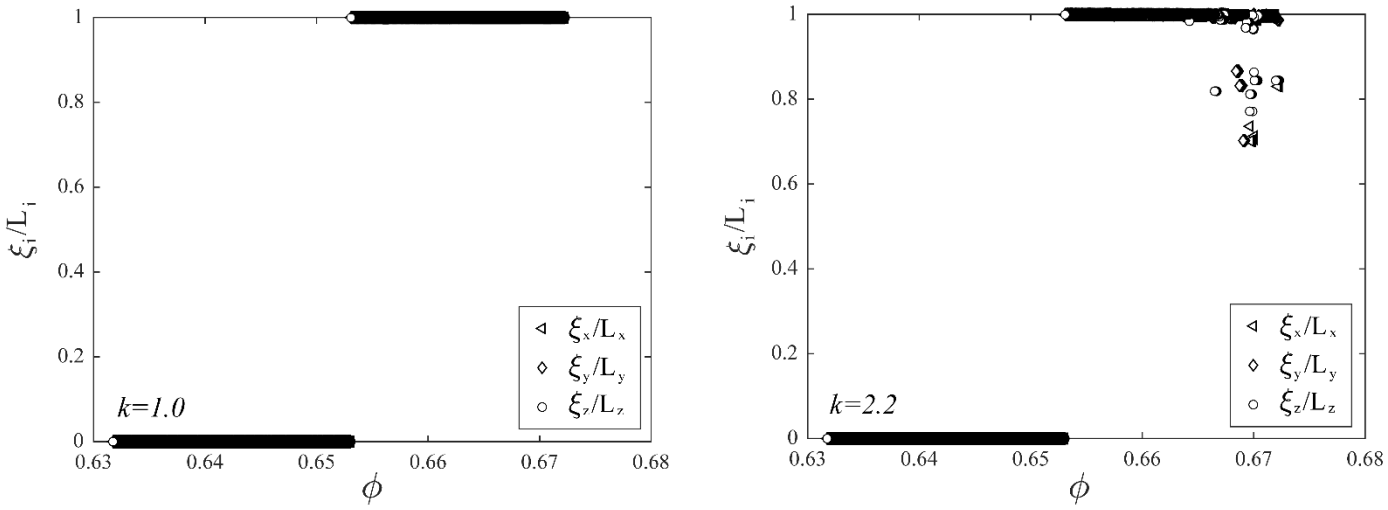

Figure 8 Percolation analysis with different k at v_r=1 during decompression for PB simulations

ϕ_J values under compression loading determined by percolation analysis with different k and different v_r are shown in Figure 9(a). ϕ_J values calculated using the C^*=6 criterion are smaller than these values from percolation analysis when $k \geq 2$ and $v_r \geq 100$. However, when $v_r < 100$, the critical solid fractions from both methods are close with $k = 2.1$. To further confirm this observation, some additional simulations were conducted with $v_r < 3$ as shown in Figure 9(b). When the compression rate is slow enough, ϕ_J determined using the C^*=6 criterion is similar to that calculated using percolation analysis of the $k = 2.1$ cluster. Figure 9 also shows that ϕ_J from percolation analysis increases with increasing v_r apart from an approximately constant regime when $v_r < 3$. Conversely, ϕ_J determined from the C^*=6 criterion decreases consistently as v_r increases. This may be because as the strain rate increases stresses tend to be concentrated in fewer particles. The particles that are not part of the k=2.1 cluster are eliminated from the percolation analysis but may be considered when calculating C^*. Figure 9 indicates that percolation analysis is not a robust method for determining jamming transition under compression loading.

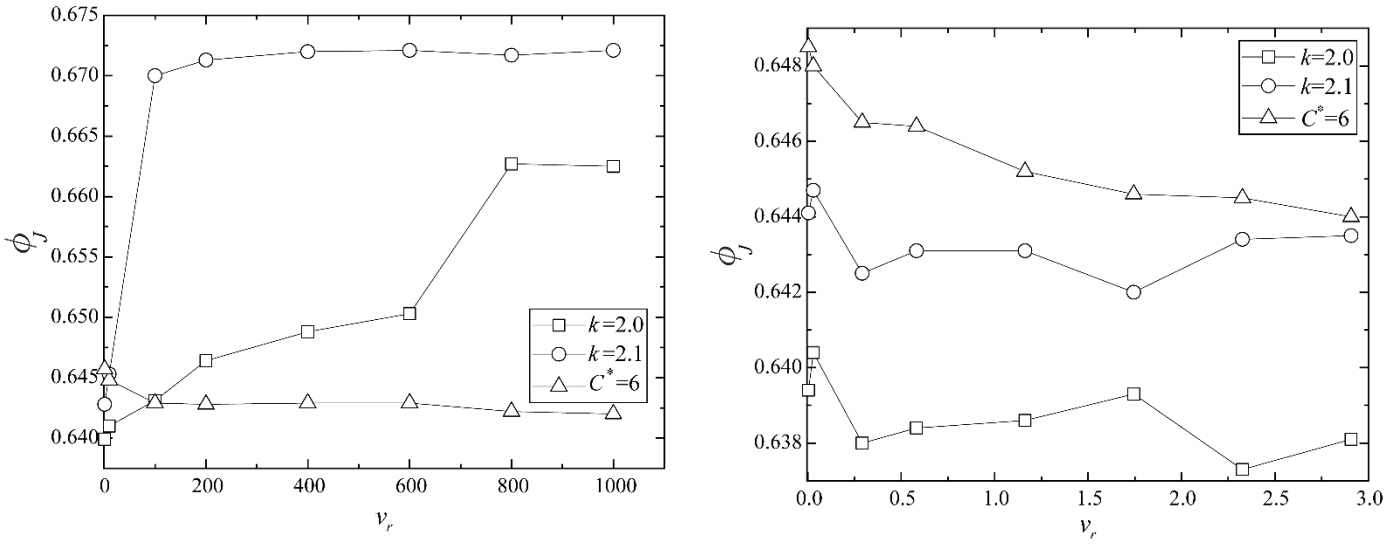

(a) Overall

(b) v_r<3

Figure 9 Comparing the critical solid fraction obtained from the C*=6 criterion with that determined from percolation analysis with different *k* values for the PB simulations during compression

The percolation analysis was also conducted for the RW simulations. The variation of ξ_i/L_i against ϕ during compression is similar to that of the PB simulations and thus is not shown for conciseness. Figure 10 is the analogue of Figure 9(a) for the RW simulations. Similar to the PB simulations, the critical solid fraction increases with increasing *k* and becomes saturated when *k* is close to 2.1. In general, the ϕ_J values determined from the C^*=6 criterion are close to those obtained by percolation analysis on the *k*=1.8 cluster. Since calculation of C^* only considers particles with more than four force-bearing contacts, the different ϕ_J values obtained using the C^*=6 criterion and percolation analysis indicate that when the compression rate is high, the external forces are concentrated in a subset of the mechanically stable particles. Figures 9 and 10 also suggest that the percolation analysis may be reliable to determine the critical solid fraction only when the compression rate is slow enough.

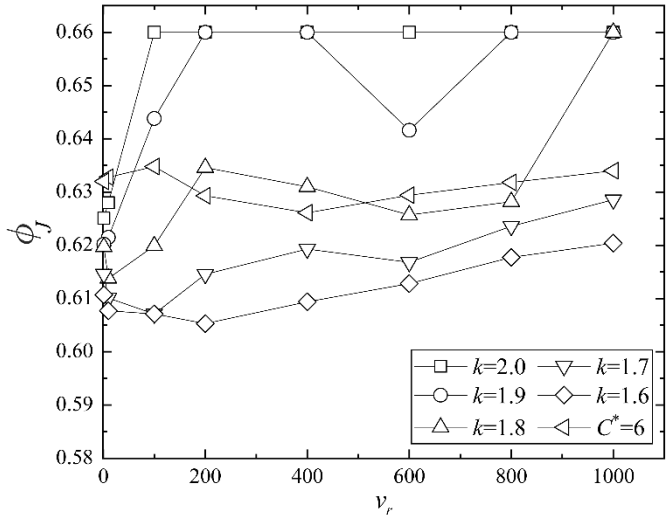

Figure 10 Percolation analysis with different *k* for the RW simulations during compression

For the decompression process, ϕ_J values using percolation analysis are listed in Table 2 for both PB and RW simulations. The decompression process can effectively reduce the dynamic influence on the force transmission structure which makes the force-bearing structure more stable. As expected, the percolation analysis under decompression conditions is less dependent on *k* compared with the compression data. For PB simulations, the identified ϕ_J is almost invariant with the *k* values for all the loading rates. However, for RW samples, the identified ϕ_J is only insensitive to *k* at very low loading rates (v_r below 10). This further indicates that the dynamic influence is more significant for RW samples than PB samples due to the high energy input at the rigid boundaries.

The application of percolation analysis to the sample shows that this method is only applicable when the force transmission structure is stable enough and *k* has little influence on the results, i.e., slow enough compression rates and the decompression process in this study.

Table 2 ϕ_J under decompression calculated using percolation analysis for PB and RW conditions

Boundary condition	v_r	ϕ_J (k=1.0)	ϕ_J (k=2.2)	ϕ_J (p=0)/C^*=6
PB	1	0.6531	0.6531	0.6533

	10	0.6533	0.6533	0.6535
	100	0.6511	0.6511	0.6514
	200	0.6511	0.6512	0.6517
	400	0.6499	0.6502	0.6506
	600	0.6489	0.6494	0.6497
	800	0.6486	0.6489	0.6494
	1000	0.6479	0.6489	0.6489
RW	1	0.6353	0.6353	0.6372
	10	0.6336	0.6344	0.6373
	100	0.6283	/	0.6436
	200	0.6273	/	0.6469
	400	0.6154	/	0.6456
	600	0.6054	/	0.642
	800	<0.6	/	0.6374
	1000	<0.6	/	0.6331

Note: In the RW condition, ϕ_J<0.6 means although the sample has already decompressed to the initial ϕ value, the largest force transmission network is still in a highly-percolated state with ξ_i/L_i>0.97.

3.3 Non-rattler fraction

Göncü et al. [8] also proposed that the fractions of rattlers can be used to determine the jamming density ϕ_J during the decompression process. Here, the modified version of this method is adopted in which the non-rattler fraction f_{NR} is used to determine ϕ_J. f_{NR} can be calculated using:

$$f_{NR} = N_4 / N \tag{6}$$

where definitions of N_4 and N are consistent with Eqs. 3 and 4. As can be seen in Figure 11, when the sample is decompressed and gets close to the jamming transition point, f_{NR} drops abruptly to zero. This indicates that the clusters having at least four contacts vanish and particles become isolated. This instant marks the occurrence of jamming transition. The ϕ_J values calculated using this method are listed in Table 3. For PB simulations, the results are nearly in accordance with those using the pressure-based method. However, when it comes to the RW condition, not all samples can get the transition point, i.e., those with v_r larger than 10 do not show an abrupt change in f_{NR}. Therefore, we cannot determine the transition point using this method for these simulations. However, for v_r = 1 and 10, the results are close to those calculated using the C^*=6 method. It can be concluded that, similar to percolation analysis, the f_{NR}-based method can only be used for slow compression rates and the decompression process.

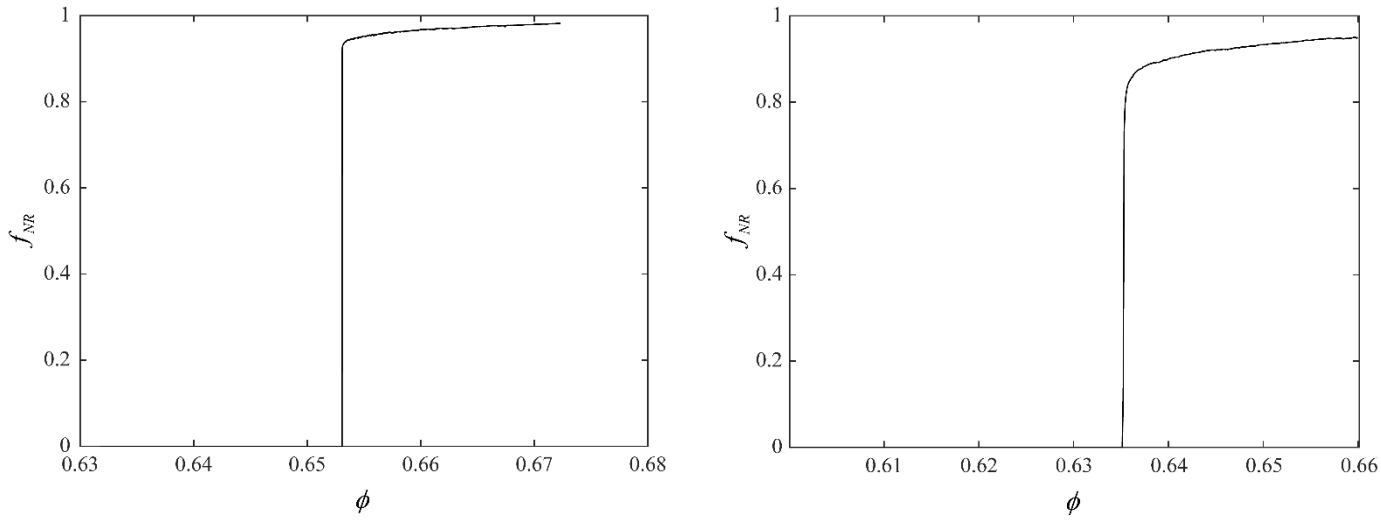

(a) PB (v_r=1) (b) RW (v_r=1)

Figure 11 Evolution of f_{NR} during decompression

Table 3 ϕ_J calculated using the f_{NR}-based criterion for PB and RW conditions under decompression

Boundary condition	v_r	ϕ_J (f_{NR})	ϕ_J (p=0)/C^*=6
PB	1	0.6531	0.6533
	10	0.6533	0.6535
	100	0.6511	0.6514
	200	0.6512	0.6517
	400	0.6501	0.6506
	600	0.6491	0.6497
	800	0.6489	0.6494
	1000	0.6487	0.6489
RW	1	0.6353	0.6372
	10	0.6348	0.6373
	100	/	0.6436
	200	/	0.6469
	400	/	0.6456
	600	/	0.642
	800	/	0.6374
	1000	/	0.6331

4 Discussion

4.1 Origin of boundary effects

As elucidated in Section 3, there exists clear differences between critical solid fractions obtained from the RW simulations and those from the PB simulations. p, C^* and f_{NR} can only give quantitative descriptions of stress and contact but cannot reflect the spatial characteristics which are directly linked to the local structure and stability of the force transmission network. In order to find the fundamental mechanism underlying these differences, the spatial characteristics of the contact and particle distributions need to be explored.

Firstly, a new parameter, the boundary particle ratio γ, is defined as the ratio between the number of particles in the major force transmission network which contact the rigid-wall boundaries (N_b) and the total number of

particles in the major force transmission network (N_f).

$$\gamma = N_b / N_f \tag{7}$$

It is used to quantitatively assess the clustering degree of particles near the boundaries. Figure 12 shows the evolution of γ during the compressing process in the RW simulations. When $v \geq 0.25$ m/s (RW-2 to RW-8), γ decreases with increasing ϕ and reaches a steady value when ϕ approaches ϕ_J. γ is larger when the compressing rate becomes higher, which indicates that particles have a higher tendency to group and move together with the rigid walls before reaching the jammed state at higher compressing rates. In contrast, when v is 0.025 m/s (RW-1), γ increases with the increase of ϕ. γ becomes almost constant approaching the jamming state. Figure 13 shows that these steady γ values, corresponding to C^*=6, increases with increasing v. The high degree of particle clustering close to the boundary makes the RW samples reach a nominal jammed state at a lower ϕ than the PB samples.

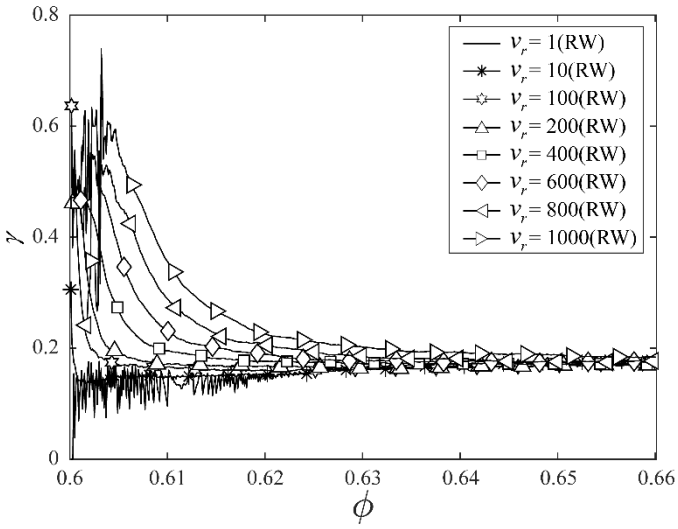

Figure 12 Boundary particle ratio against solid fraction with RW boundary conditions

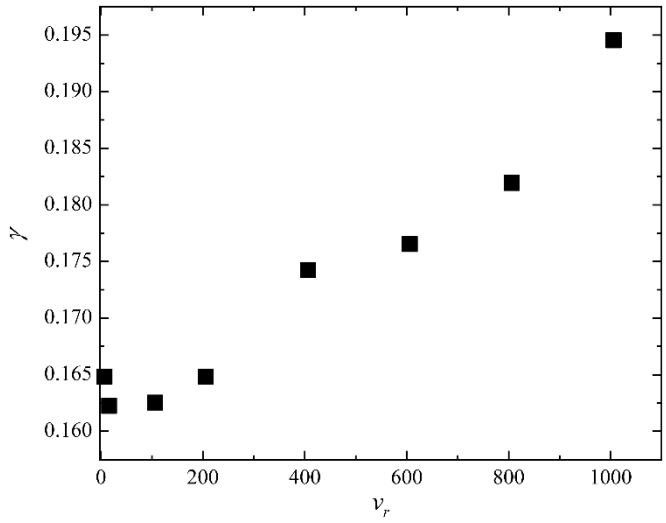

Figure 13 Steady boundary particle ratio at different compressing rates

To further analyze the non-uniformity of particle distribution induced by different boundary conditions, the sample is divided into ten regions according to the distance d of the external boundary with respect to the center, i.e., d/D = 0.1 to 1, as shown in Figure 14. Each region is the difference set of the inner and the outer cubic boxes.

The solid fraction of each region is calculated at an initial state (unjamming state) close to the jamming transition point (C^*=0), the jamming transition point (C^*=6/p=0) and a jammed state (C^*=6.5) for all strain rates and boundary conditions (Figures 15 and 17 for compression and decompression, respectively). Statistical features of ϕ for different v_r can be seen in Figures 16 and 18 for compression and decompression, respectively. The volume of a particle located between regions is partitioned appropriately to each region's solid volume. Generally, the distribution of solid fraction in the PB simulations is nearly uniform at all instants and no compression rate dependency is observed for both compression and decompression. The distribution is more heterogeneous in the RW simulations.

For the compression process, at the initial state the particles aggregate close to the boundaries and the solid fraction decreases gradually from the boundaries to the center. The differences in solid fraction between regions become more pronounced as compression rate decreases. Distributions at the jamming transition point and the jammed state are similar to those at the initial state except that the solid fractions at the boundary and center become more similar as the sample is more closely packed. This is different from Huang et al. [26] who observed that, subjected to shearing, the sample is more loosely packed close to the RW boundaries. The distributions of solid fraction for the RW-1 and RW-2 simulations at the jamming transition state and those for RW-1, RW-2 and RW-3 simulations at the jammed state become similar to the distribution of PB samples. Therefore, it is reasonable to expect that the distribution of solid fraction in the simulations with higher strain rates will also become similar to that of PB samples as the degree of jamming is increased, i.e., with a higher C^*. When the solid fraction distributions at the initial and jammed states (Figure 15 (a) and (c)) are compared, a clear increase of the solid fraction can be seen in the central part. Furthermore, at the jammed state, when the compression rate is slow enough, the solid fraction in the central part is the largest compared with the other parts in the sample. This may indicate that the different observations between the current study at high compression rates and Huang et al. [26] is due to the different degrees of jamming as in Huang et al. [26] all the samples were in highly jammed states.

It is now clear that the homogeneity of packing density for PB simulations does not depend on loading rate and jamming state. However, for RW simulations, the homogeneity of packing density depends on both loading rate and loading state. In an unjammed state in which the particles are sparsely distributed within a large domain, a higher loading rate leads to higher impact energy at the boundary which propagates further, i.e., the particle-RW interaction is dominant. Therefore, the larger range of particles close to the boundaries will be compacted subject to higher compression rate, thereby inducing smaller discrepancies. With increasing closeness between particles (i.e., increasing degree of percolation) when the system evolves from unjamming to jamming states, the compression at the boundaries can be more easily 'felt' and propagated into the internal regions. A smaller loading rate will be beneficial for particle rearrangement, which leads to a more homogeneous packing. Therefore, at the jammed state with the same C^* the solid fraction increases but its discrepancy decreases with decreasing loading rate.

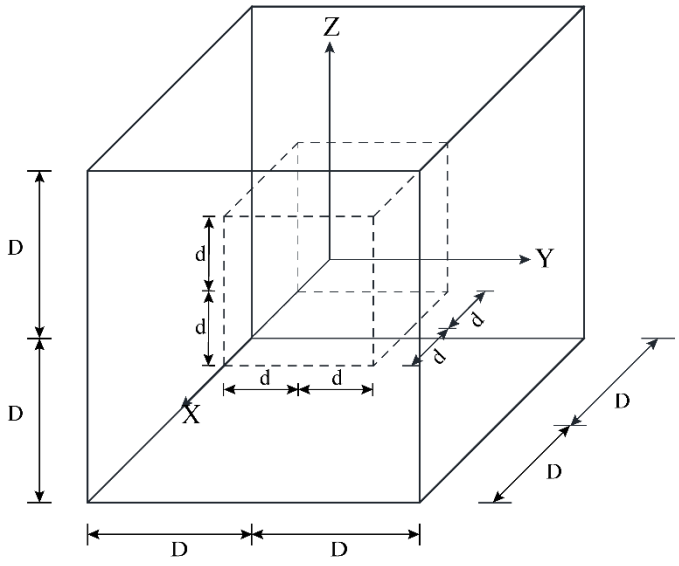

Figure 14 Division of the box

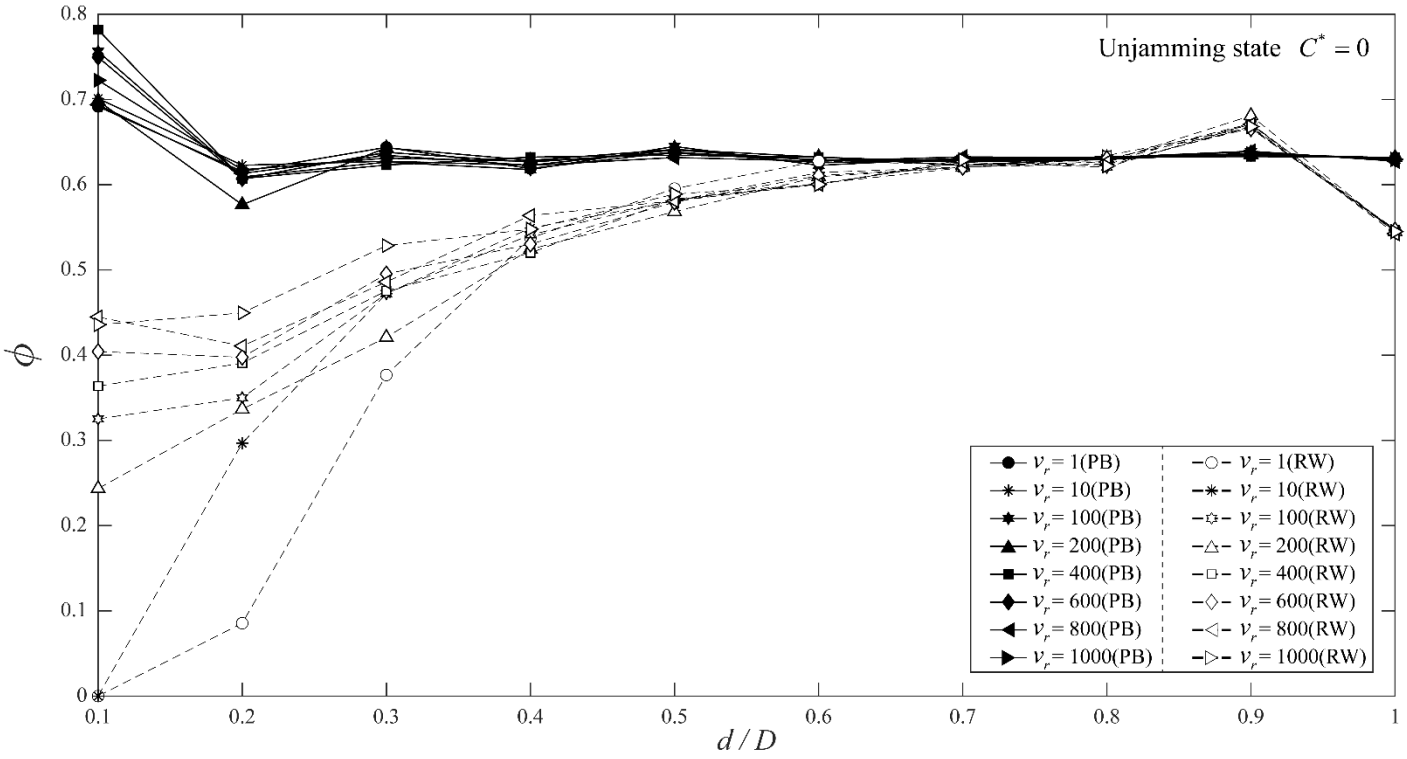

(a) Distribution of solid fraction in different sample regions at the initial state (C^*=0)

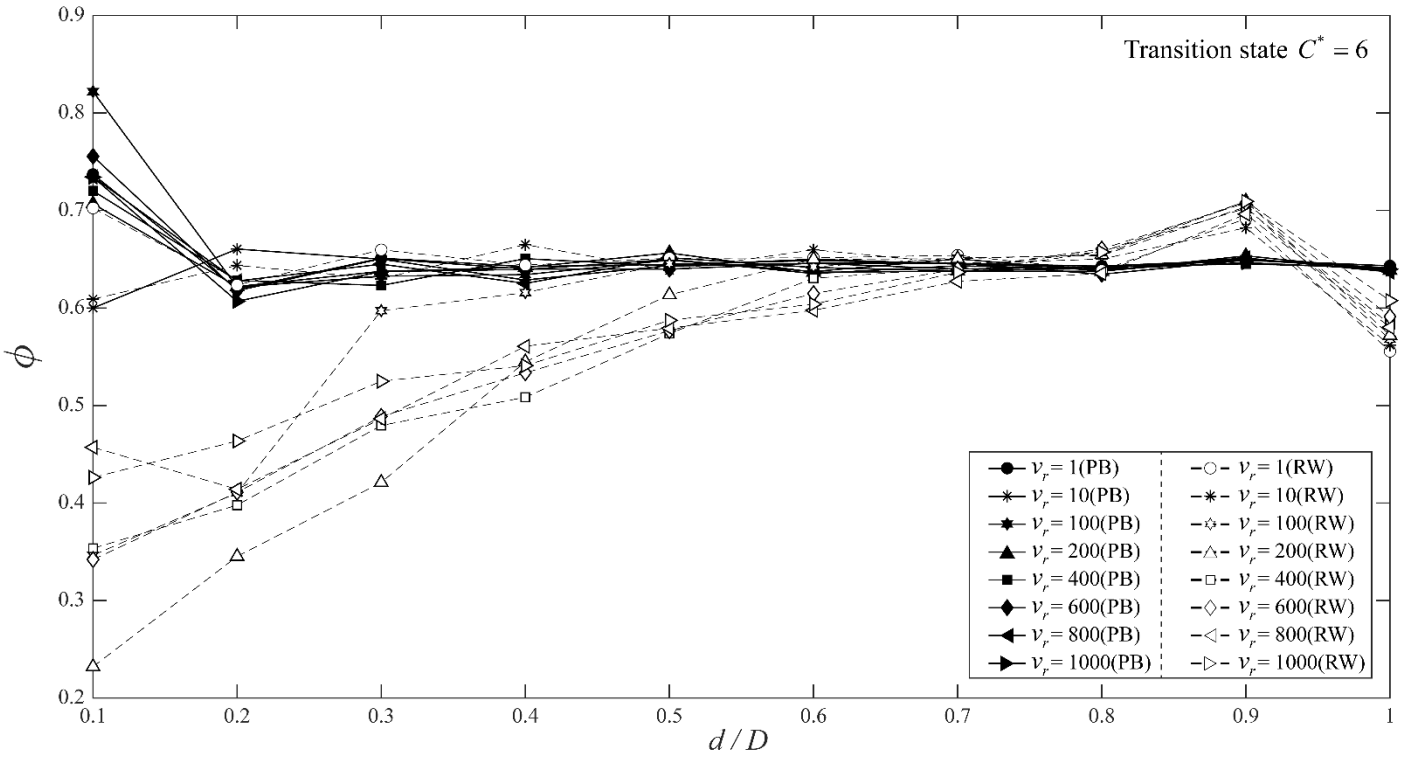

(b) Distribution of solid fraction in different sample regions at the jamming point (C^*=6)

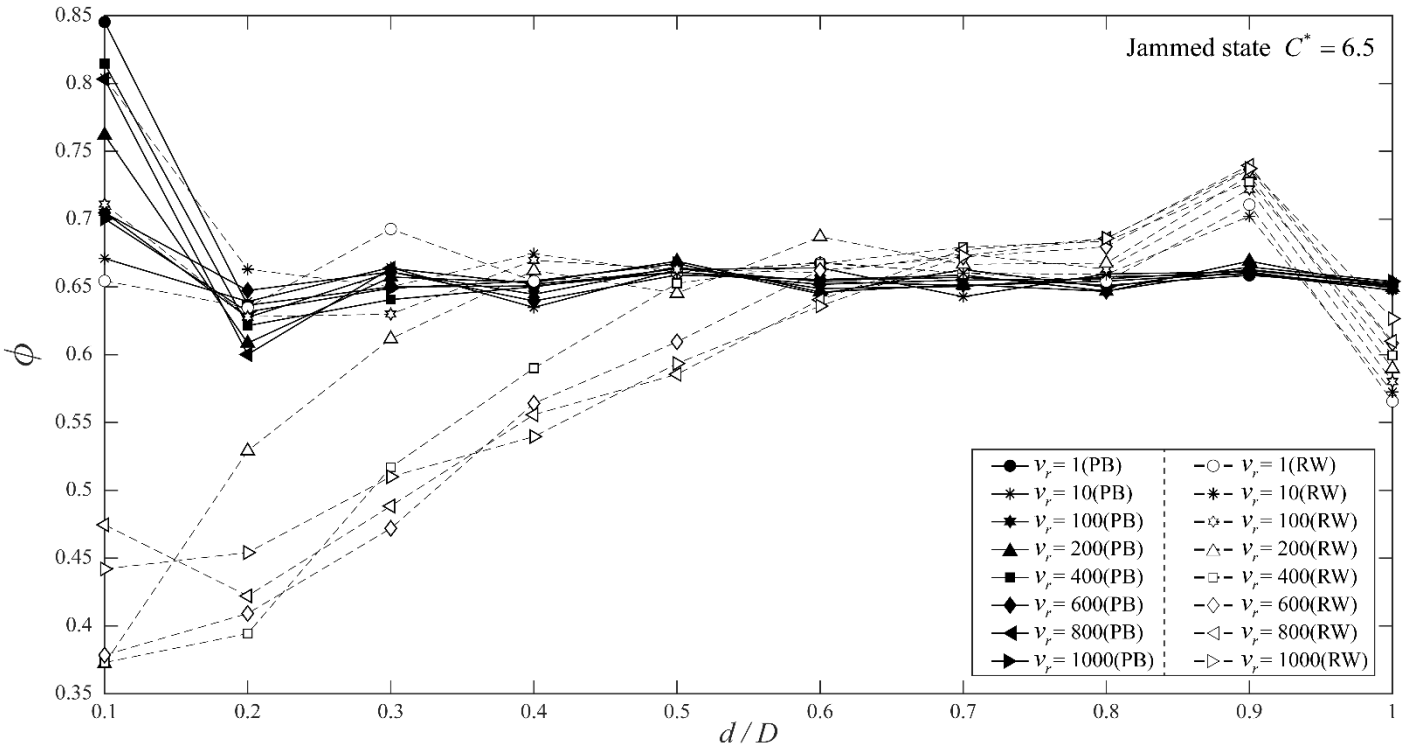

(c) Distribution of solid fraction in different sample regions at the jammed state (C^*=6.5)

Figure 15 Distribution of solid fraction within the sample during compression

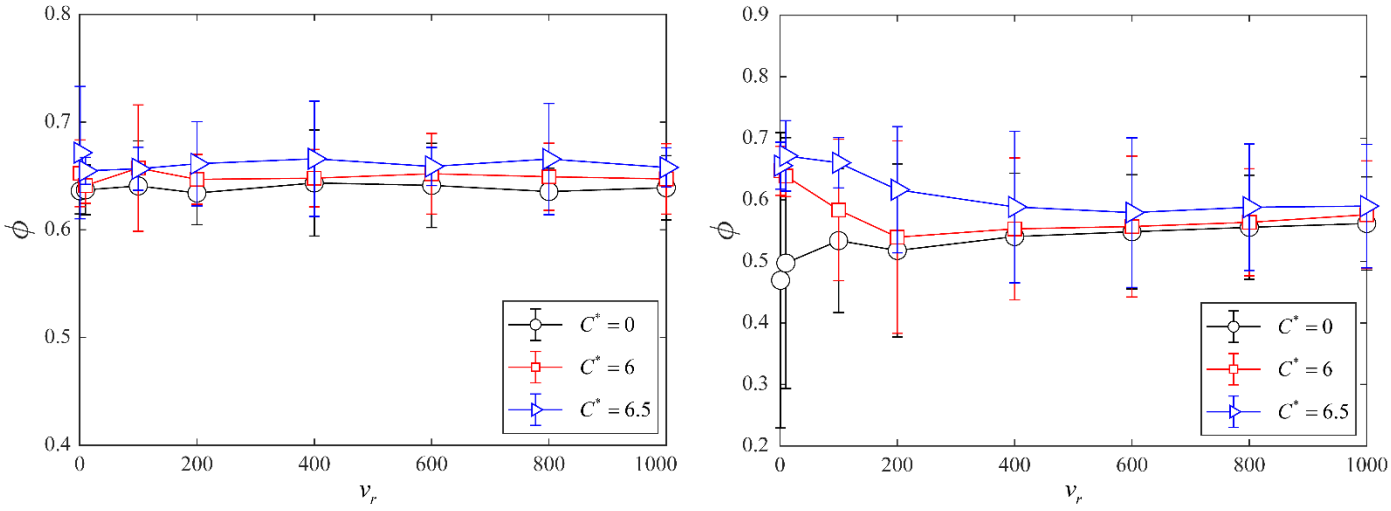

(a)PB (b)RW

Figure 16 Mean value and standard deviation of solid fraction distribution within the sample during compression

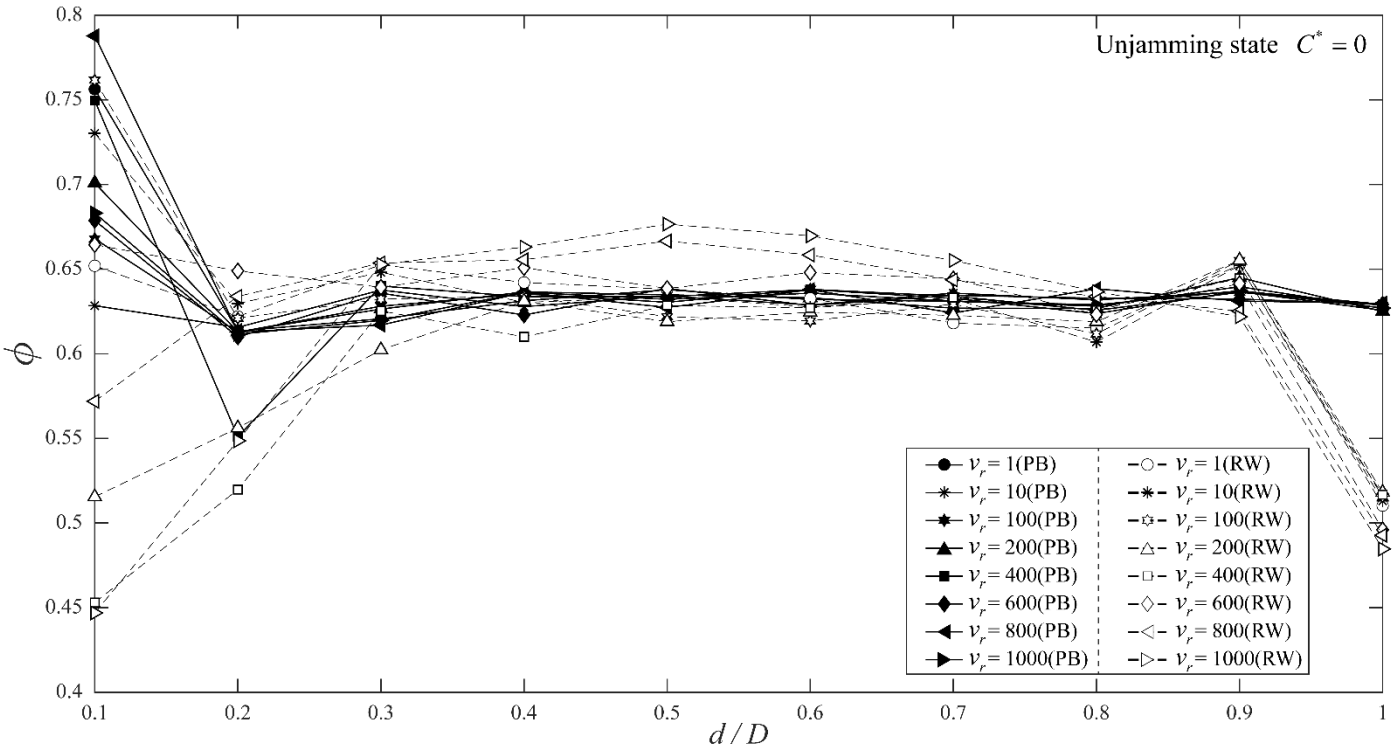

(a) Distribution of solid fraction in different sample regions at the unjamming state

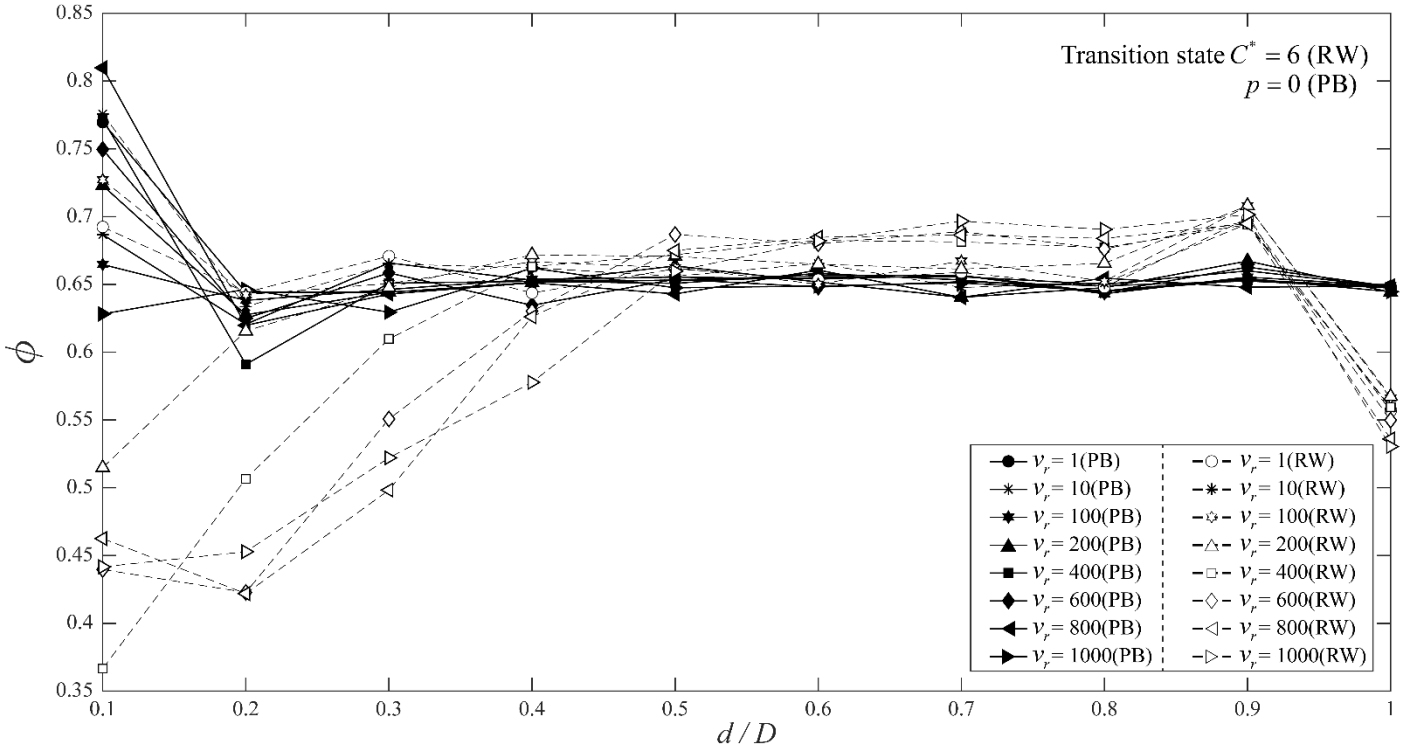

(b) Distribution of solid fraction in different sample regions at the jamming point

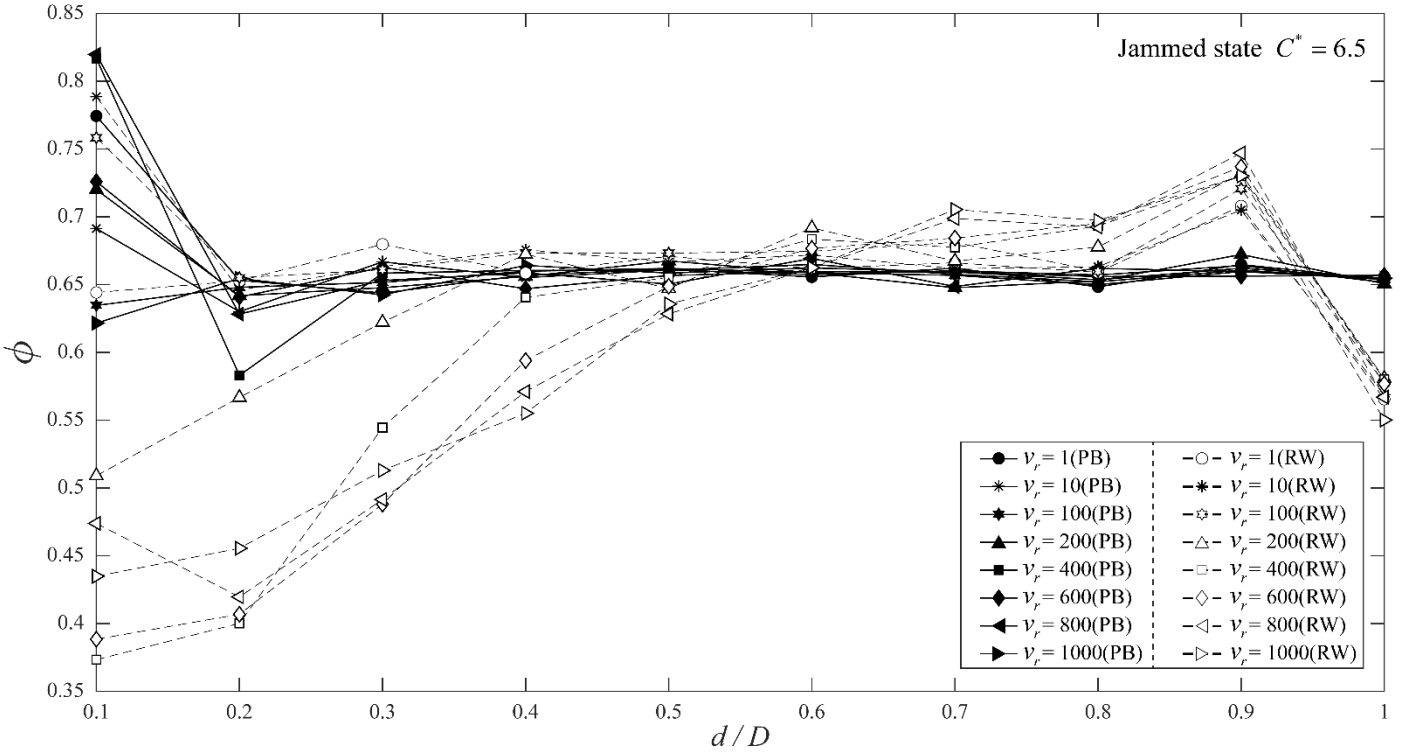

(c) Distribution of solid fraction in different sample regions at the jammed state

Figure 17 Distribution of solid fraction within the sample during decompression

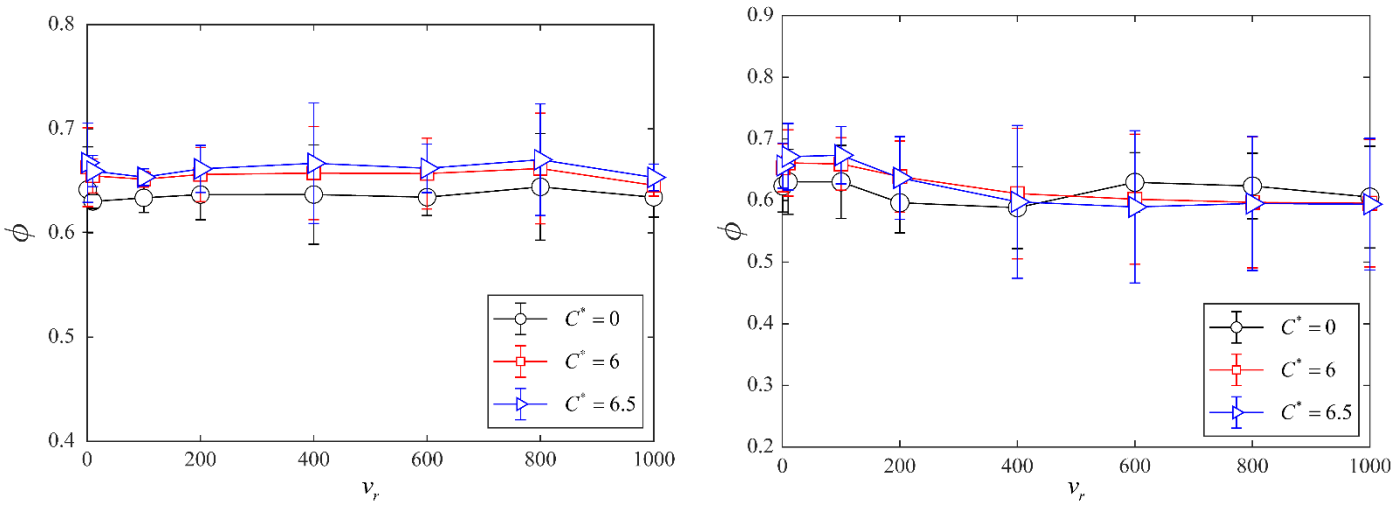

(a)PB (b)RW

Figure 18 Mean value and standard deviation of solid fraction distribution within the sample during decompression

The critical solid fractions determined using the pressure-based criterion are also calculated considering the cubic central part of the sample (d/D≤0.9) under RW conditions. As shown in Figure 19, when only the more homogeneous inner regions are considered to determine the ϕ_J, the RW data get closer to those under PB conditions.

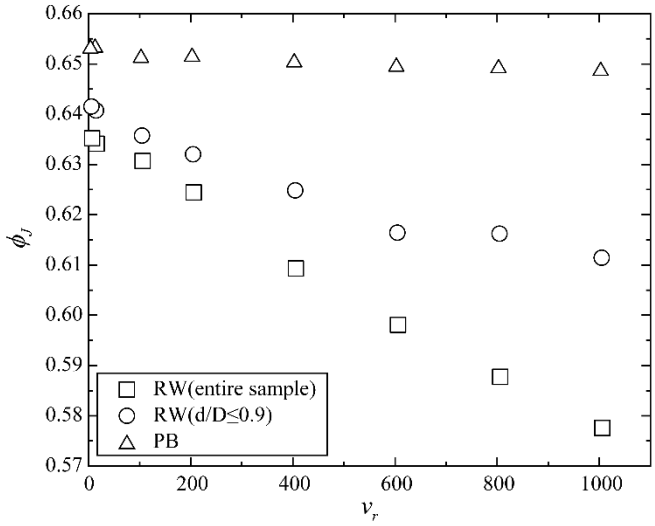

Figure 19 Comparing ϕ_J of RW simulations obtained considering homogeneous inner regions with those obtained for the entire RW samples and PB samples

The distribution of the solid fraction has clearly shown that rigid-wall boundaries can have a strong influence on the distribution of the particles when the sample is not large enough. In order to better illustrate this system-size dependent problem, further simulations were conducted with numbers of particles, N=40000,80000,120000 under RW conditions with the fastest compression rate, which exhibits the strongest boundary effect. As shown in Table 4, the critical solid fraction obtained in unloading approaches that obtained in PB simulations. We can

expect closer agreement if only the inner homogeneous regions were considered when calculating ϕ_J.

Table 4 Comparing the critical solid fraction of RW samples containing different numbers of particles with that of the PB sample

	RW N=20000	RW N=40000	RW N=80000	RW N=120000	PB N=20186
ϕ_J	0.5782	0.5869	0.5915	0.5925	0.6489

4.2 Explanation for the strain rate dependency

As observed in Section 3, the sample compressed at a higher strain rate reaches the jammed state earlier with a smaller critical solid fraction in both the RW and PB simulations. In order to explain this phenomenon, the stability and statistical features of the force transmission network are analyzed in this section.

Figure 20 shows the distribution of particles' connectivity. In general, the sample loaded at a slower compression rate has a higher proportion of particles with connectivity ≥ 4 (Figure 20(a)). It means that when the sample is isotropically compressed at a slower strain rate, the force transmission network contains more mechanically stable particles and should be more stable than that of samples isotropically compressed at a larger strain rate. Similar observations can be made for the PB samples, but the difference in the distribution of particles' connectivity in the PB simulations is less pronounced than in the RW simulations (Figure 20(b)). This explains why the critical solid fraction determined from percolation analysis increases with increasing v_r in Figure 9 and Figure 10.

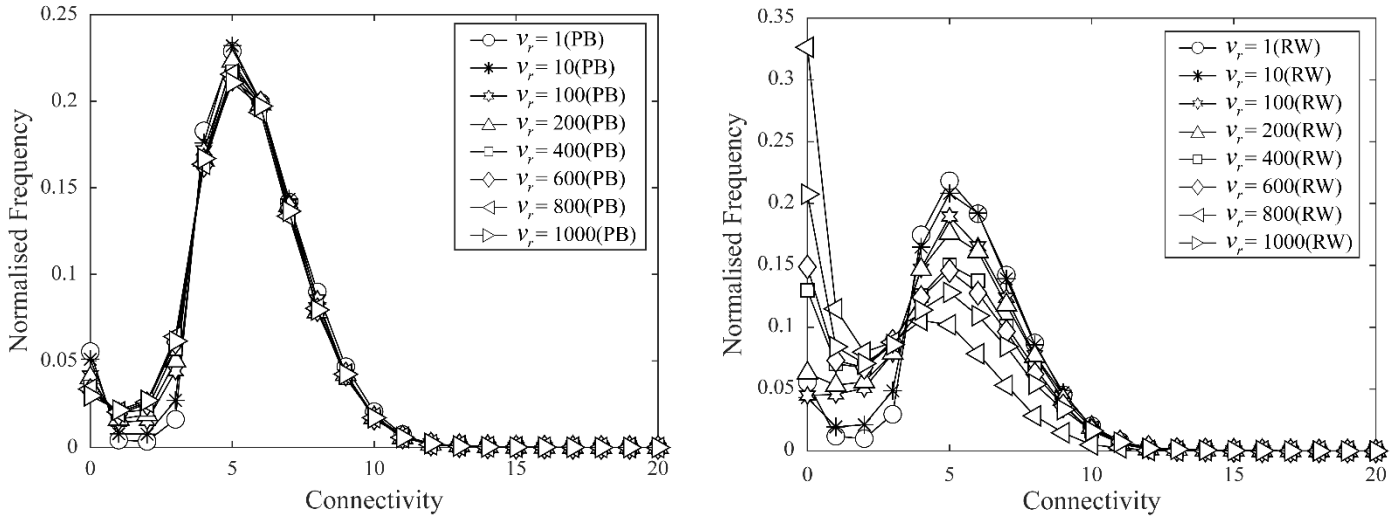

(a) Periodic boundary (b) Rigid-wall boundary

Figure 20 Distribution of particle connectivity

The contribution of the largest cluster to the normalized overall mean stress p is calculated for both boundary conditions at the jamming transition state (Figure 21). The largest cluster is determined by searching through the contact network of particles having at least 4 neighboring particles. For both boundary conditions, the largest cluster contributes less to p with increasing compression rate, which means that when the sample is isotropically compressed at a slower strain rate, the largest cluster contains more mechanically stable particles and thus sustains a larger proportion of external force, in line with Figure 20.

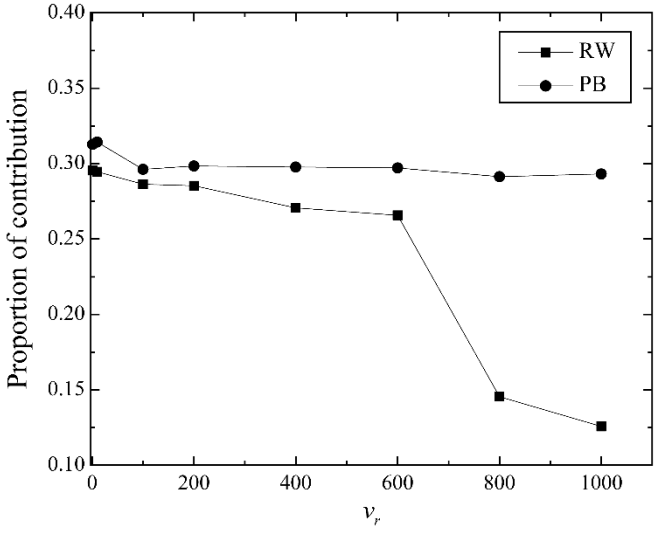

Figure 21 Contributions of largest clusters to the overall mean stress p

The stability of the force transmission network can also be reflected from its temporal variation during relaxation. The samples are relaxed for 100000 timesteps without a change of the boundary positions. p is plotted against timestep during relaxation as shown in Figure 21. In the PB simulations, the faster the compression rate v is, the larger the initial p is and the more quickly p drops (Figure 22(a)). A similar tendency can be seen in the RW simulations in Figure 22(b). This tendency implies that although the faster compression rate results in a larger p at the jamming state, the force transmission network is less stable compared with that under the slower compression rate condition. However, some difference between the PB and RW simulations still can be observed. In the PB simulations, p can drop nearly to zero while in the RW simulations the residual p is still significant except for v_r=400 (RW). This may be because the rigid-wall sample may not be at its exact point of jamming transition. Figure 23 shows the change in the proportion of persistent contacts which exist both at the beginning of relaxation and the recording timestep of interest, including the small fraction of contacts which are lost and re-formed during that time interval. With the decrease of compression rate, there are more persistent contacts, implying that the force transmission network is more stable at a slower than at a faster compression rate. For v_r=400-1000 (PB), almost all contacts are lost after relaxation for 40000 timesteps, whereas for RW samples except for v_r=400 (RW), a large proportion of contacts survive after relaxation. This explains why the residual stress in RW samples is much larger than that in PB samples (Figure 22).

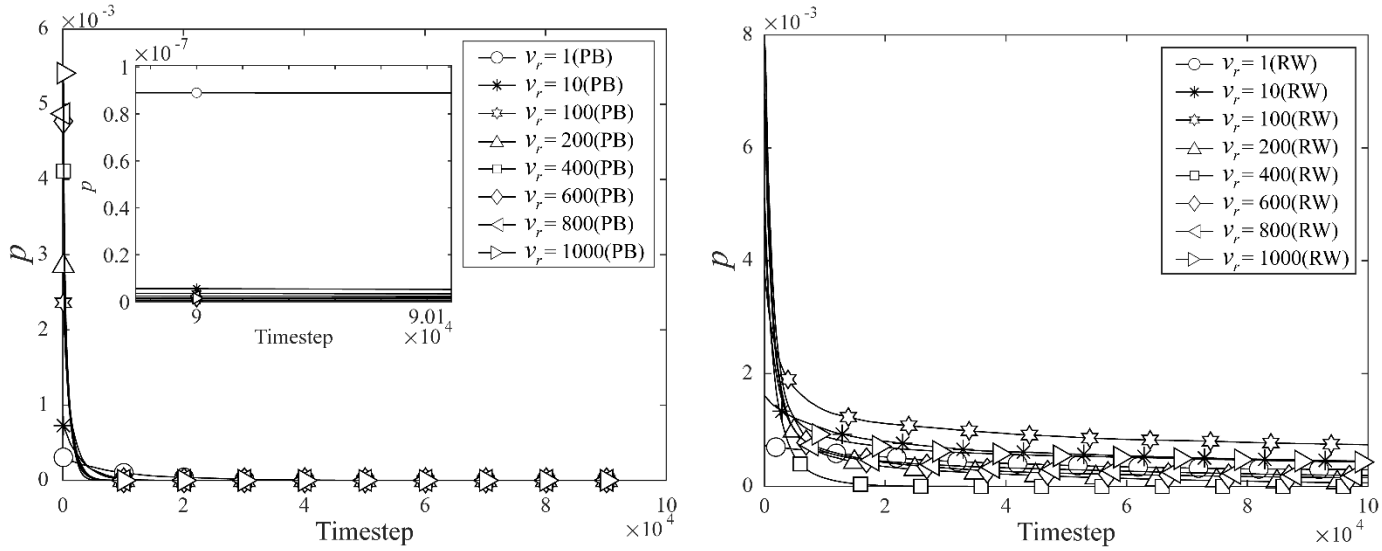

(a) periodic boundary condition (b)rigid-wall boundary condition

Figure 22 Dimensionless p during relaxation at the jamming transition state

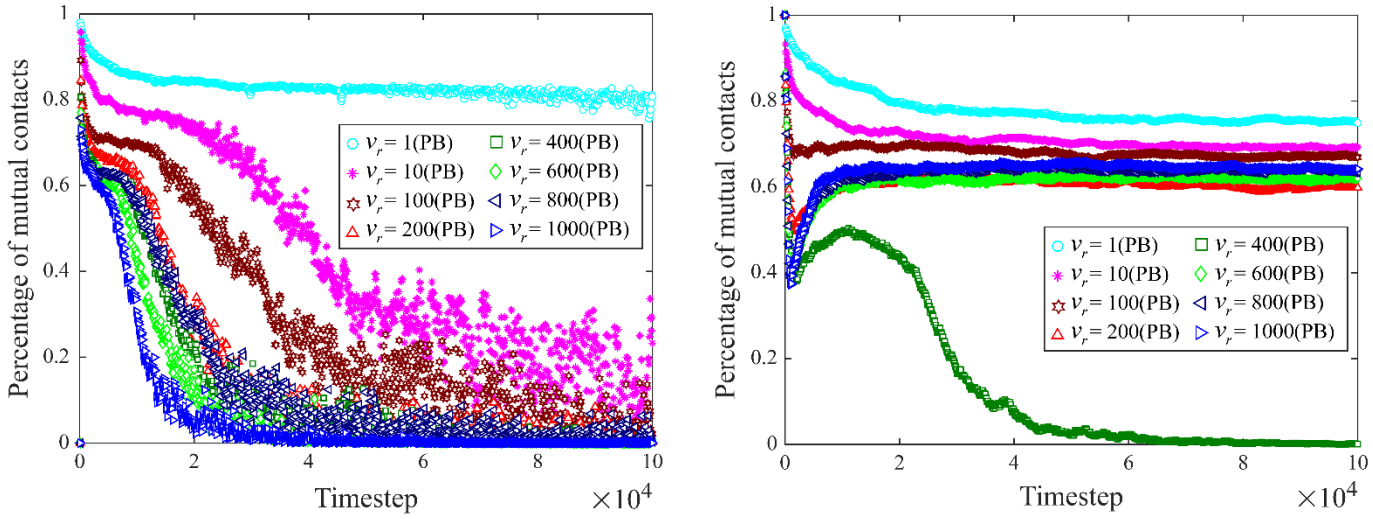

(a) PB condition (b) RW condition

Figure 23 Contact comparison during relaxation at the jamming transition state

The stability and homogeneity of the force transmission network is the key to the strain rate dependency. A faster compression rate results in a smaller critical solid fraction with a less stable force transmission network. The resultant jamming state under high compression rates is a transient isostatic state compared with that resulting from a slower compression rate.

4.3 Correlations between dynamics and homogeneity

As aforementioned, although the decompression process has been adopted to reduce the dynamics when determining ϕ_J, its influence cannot be fully eliminated, especially for the comparatively fast compression rate conditions. Moreover, the dynamic effect is more notable for the RW samples than for the more homogeneous PB samples. This implies that the system's dynamics is correlated with the sample's homogeneity, which is the origin of observed discrepancies between RW simulations and PB simulations. To further illustrate this, we

compare the overall ϕ_J values with those obtained within the interior regions for samples with different numbers of particles under the highest strain rate condition (Figure 24). It is clear that the dynamic effect decreases as the sample size increases. Therefore, the dynamic effects in jamming analyses can be reduced by either increasing the sample size or by using a compression rate much smaller than the ones used in the current study. A compromise compatible with the computation cost may be achieved by an appropriate combination of the two.

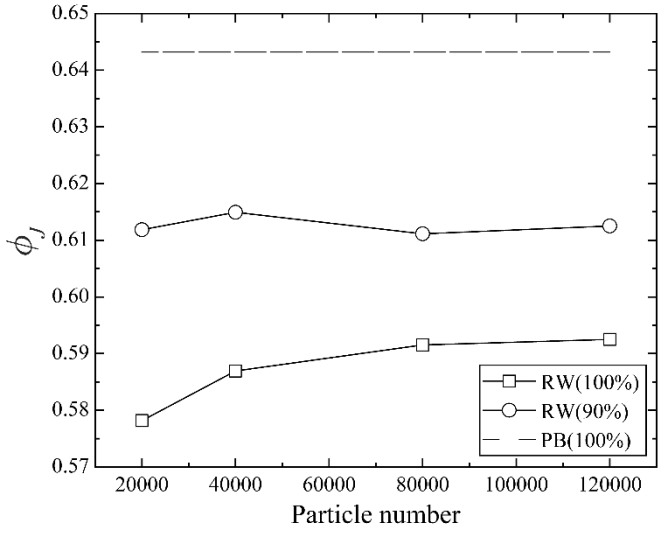

Figure 24 Reduction of dynamic effects with increasing sample size (v_r=1000)

5 Conclusion

The non-uniqueness of the critical solid fraction at the jamming state considering both rigid-wall (RW) and periodic (PB) boundary conditions and the strain rate effects have been systematically studied in this paper. The relationships between the dimensionless confining pressure p, the corrected coordination number C^*, critical solid fraction ϕ_J and strain rate v were analyzed. Special attention was paid to temporal alterations in and the stability of the force transmission network, which are key to explain the strain rate dependency.

Of all the existing methods, the pressure-based criterion is the most reliable one to determine the jamming transition density. Regardless of the approach used, the RW simulations give a range of critical solid fraction that is smaller than the PB simulations. Compression leads to more notable dynamic effects than decompression. The RW samples are more susceptible to dynamic effects due to the high input energy at the rigid boundaries. The strain-rate dependency of the critical solid fraction is more significant in the RW case than in the PB case. Particles tend to cluster close to the RW boundaries at high compression rates, leading to nonuniform distributions of solid fraction. This is the origin of the different critical solid fractions obtained from the RW and PB simulations. The nonuniformity becomes less pronounced and the solid fraction distribution in the interior regions of RW samples approaches that of PB samples as the compression rate decreases. In both RW and PB simulations, the external forces are more concentrated in strong contacts and the force transmission network is temporal and more variable as the compression rate increases. This leads to a less stable force transmission network which causes the sample to jam at a smaller critical solid fraction in simulations with higher compression rates. The effects of dynamics and inhomogeneity on the jamming behavior are coupled. A prudent examination of the critical solid fraction using DEM can be achieved only when the strain rate is low enough and a homogeneous sample is employed.

Future efforts will be devoted to the accurate identification of the complete jamming diagram by adhering to the findings and observations noted in the current study, which will also provide valuable guidance for future studies on other aspects of jamming behavior using DEM.

Acknowledgement

The research was funded by the National Natural Science Foundation of China (No. 51509186 and 41877227) and the National Key Research and Development Program of China (2017YFC0806004).

Reference

[1] Liu, A. J., & Nagel, S. R. (1998). Nonlinear dynamics: Jamming is not just cool any more. Nature, 396(6706), 21–22. https://doi.org/10.1038/23819

[2] Bi, D., Zhang, J., Chakraborty, B., & Behringer, R. P. (2011). Jamming by shear. Nature, 480(7377), 355–358. https://doi.org/10.1038/nature10667

[3] Liu, A. J., & Nagel, S. R. (2010). Granular and jammed materials. Soft Matter, 6(13), 2869. https://doi.org/10.1039/c005388k

[4] Ciamarra, M. P., Pastore, R., Nicodemi, M., & Coniglio, A. (2011). Jamming phase diagram for frictional particles. Physical Review E - Statistical, Nonlinear, and Soft Matter Physics, 84(4). https://doi.org/10.1103/PhysRevE.84.041308

[5] Liu, A. J., & Nagel, S. R. (2010). The Jamming Transition and the Marginally Jammed Solid. Annual Review of Condensed Matter Physics, 1(1), 347–369. https://doi.org/10.1146/annurev-conmatphys-070909-104045

[6] Vinutha, H. A., & Sastry, S. (2016). Disentangling the role of structure and friction in shear jamming. *Nature Physics*, *12*(6), 578–583. https://doi.org/10.1038/nphys3658

[7] Kumar, N., & Luding, S. (2016). Memory of jamming–multiscale models for soft and granular matter. *Granular Matter*, *18*(3), 1–21. https://doi.org/10.1007/s10035-016-0624-2

[8] Göncü, F., Durán, O., & Luding, S. (2009). Jamming in frictionless packings of spheres: Determination of the critical volume fraction. AIP Conference Proceedings, 1145(1), 531–534. https://doi.org/10.1063/1.3179980

[9] Göncü, F., Durán, O., & Luding, S. (2010). Constitutive relations for the isotropic deformation of frictionless packings of polydisperse spheres. Comptes Rendus - Mecanique, 338(10–11), 570–586. https://doi.org/10.1016/j.crme.2010.10.004

[10] Hartley, R. R., & Behringer, R. P. (2003). Logarithmic rate dependence of force networks in sheared granular materials. *Nature*, *421*(6926), 928–931. https://doi.org/10.1038/nature01394

[11] Zhang, H. P., & Makse, H. A. (2005). Jamming transition in emulsions and granular materials. Physical Review E - Statistical, Nonlinear, and Soft Matter Physics, *72*(1), 1–12. https://doi.org/10.1103/PhysRevE.72.011301

[12] Mari, R., Krzakala, F., & Kurchan, J. (2009). Jamming versus glass transitions. *Physical Review Letters*, *103*(2), 1–4. https://doi.org/10.1103/PhysRevLett.103.025701

[13] Donev, A., Stillinger, F. H., & Torquato, S. (2006). Do binary hard disks exhibit an ideal glass transition? *Physical Review Letters*, *96*(22), 1–4. https://doi.org/10.1103/PhysRevLett.96.225502

[14] Speedy, R. J. (1994). On the reproducibility of glasses. *The Journal of Chemical Physics*, *100*(9), 6684–6691. https://doi.org/10.1063/1.467028

[15] Ogarko, V., & Luding, S. (2012). Equation of state and jamming density for equivalent bi- and polydisperse, smooth, hard sphere systems. Journal of Chemical Physics, 136(12). https://doi.org/10.1063/1.3694030

[16] Vågberg, D., Olsson, P., & Teitel, S. (2011). Glassiness, rigidity, and jamming of frictionless soft core disks. *Physical Review E - Statistical, Nonlinear, and Soft Matter Physics*, *83*(3), 1–9. https://doi.org/10.1103/PhysRevE.83.031307

[17] Otsuki, M., & Hayakawa, H. (2011). Critical scaling near jamming transition for frictional granular particles. *Physical Review E - Statistical, Nonlinear, and Soft Matter Physics*, *83*(5), 5–10.

https://doi.org/10.1103/PhysRevE.83.051301
[18] Marketos, G., & Bolton, M. D. (2009). Flat boundaries and their effect on sand testing. International Journal for Numerical and Analytical Methods in Geomechanics, 30(13), 821-837. https://doi.org/10.1002/nag.835
[19] Itasca Consulting Group. Particle Flow Code in Three Dimensions: User's Manual, Version 4.0. Minneapolis, USA 2007
[20] Plimpton S. (1995) Fast parallel algorithms for short-range molecular dynamics. *Journal of Computational Physics*, 117, 1–19. doi: 10.1006/jcph.1995.1039
[21] Majmudar, T. S., Sperl, M., Luding, S., & Behringer, R. P. (2007). Jamming transition in granular systems. *Physical Review Letters*, *98*(5), 1–4. https://doi.org/10.1103/PhysRevLett.98.058001
[22] Imole, O. I., Kumar, N., Magnanimo, V., & Luding, S. (2012). Hydrostatic and shear behavior of frictionless granular assemblies under different deformation conditions. *KONA Powder and Particle Journal*, *30*(August 2016), 84–108. https://doi.org/10.14356/kona.2013011
[23] Radjai, F., Wolf, D., Jean, M., & Moreau, J. J., (1998). Bimodal Character of Stress Transmission in Granular Packings. *Physical Review Letters, American Physical Society*, *80*(1), 61–64. https://doi.org/10.1103/PhysRevLett.80.61
[24] Hidalgo, R. C., Grosse, C. U., Kun, F., Reinhardt, H. W., & Herrmann, H. J. (2002). Evolution of Percolating Force Chains in Compressed Granular Media. *Physical Review Letters*, *89*(20), 1–5. https://doi.org/10.1103/PhysRevLett.89.205501
[25] Smith, K. C., Fisher, T. S., & Alam, M. (2011). Isostaticity of constraints in amorphous jammed systems of soft frictionless Platonic solids. *Physical Review E - Statistical, Nonlinear, and Soft Matter Physics*, *84*(3). https://doi.org/10.1103/PhysRevE.84.030301
[26] Huang, X., Hanley, K. J., O'Sullivan, C., & Kwok, F. C. Y. (2014). Effect of sample size on the response of DEM samples with a realistic grading. *Particuology*, *15*, 107–115. https://doi.org/10.1016/j.partic.2013.07.006